

Evolution model for the Absheron Mud Volcano: from stratified sediments to fluid mud generation

Arthur Blouin¹, Nabil Sultan², Alexandra Pierron², Patrice Imbert³, and jean-paul callot³

¹Ifremer

²IFREMER

³LFCR IPRA

November 24, 2022

Abstract

We propose a semi-quantitative model of the initiation and early evolution of a mud volcano. Basin modeling was calibrated against our previous seismic interpretation of the Absheron mud volcano and surroundings in the South Caspian Basin on the one hand, analysis of geological samples from seabed and two exploration boreholes on the other. Some input parameters of the model were derived from laboratory testing of samples from the mud volcano and we used a constitutive law obtained from a previous laboratory study showing the extent to which gas exsolution may damage host sediments, eventually leading to mud generation from compacted sediments. The study identified key geological and physical conditions that led to mud volcano formation: coupling diffusion processes with hydrofracturing and fluid advection, we were able to simulate conditions required to generate mud 3.5 km below the Absheron mud volcano. We also modeled mud remobilization up to the seabed using Navier-Stokes equations modified to account for the impact of gas expansion on mud density. Considering density inversion only, simulations indicate that mud would be extruded at the seabed 100 years after its generation, an ascent rate similar to extrusion rates measured at some active mud volcanoes in Azerbaijan, e.g. the Kotyrdag mud volcano. These models considering eruption dynamics provide semi-quantitative support to purely conceptual formation models based on seismic interpretation of subvolcanic stratal geometry.

1 **Evolution model for the Absheron Mud Volcano: from stratified sediments to**
2 **fluid mud generation**

3 **Arthur Blouin^{1,2,3}, Nabil Sultan¹, Alexandra Pierron¹, Patrice Imbert³,**
4 **Jean-Paul Callot³**

5 ¹ Ifremer, Lab. Aléas Géologiques et Dynamiques Sédimentaires, Géosciences Marines, REM,
6 Centre de Bretagne, Pointe du Diable, 29280 Plouzané.

7 ² R&D/EP Total S.A., Avenue Larribau, 64000 Pau.

8 ³ Université de Pau et des Pays de l'Adour, E2S UPPA, CNRS, TOTAL, Avenue de l'Université,
9 64013 Pau cedex, France

10 Corresponding author: Arthur Blouin (a.blouin@fugro.com)

11 **Key Points:**

- 12 • Simulation of mud generation is possible through regional 2D-diffusion modeling
- 13 • Mud ascent through gas-expansion-driven density inversion is possible, although
- 14 additional processes may accelerate the phenomenon.
- 15 • Numerical modeling results allow proposing a semi-quantitative formation model
- 16 for the Absheron mud volcano.

17 **Abstract**

18 We propose a semi-quantitative model of the initiation and early evolution of a mud
19 volcano. Basin modeling was calibrated against our previous seismic interpretation of the
20 Absheron mud volcano and surroundings in the South Caspian Basin on the one hand, analysis of
21 geological samples from seabed and two exploration boreholes on the other. Some input
22 parameters of the model were derived from laboratory testing of samples from the mud volcano
23 and we used a constitutive law obtained from a previous laboratory study showing the extent to
24 which gas exsolution may damage host sediments, eventually leading to mud generation from
25 compacted sediments. The study identified key geological and physical conditions that led to
26 mud volcano formation: coupling diffusion processes with hydrofracturing and fluid advection,
27 we were able to simulate conditions required to generate mud 3.5 km below the Absheron mud
28 volcano. We also modeled mud remobilization up to the seabed using Navier-Stokes equations
29 modified to account for the impact of gas expansion on mud density. Considering density
30 inversion only, simulations indicate that mud would be extruded at the seabed 100 years after its
31 generation, an ascent rate similar to extrusion rates measured at some active mud volcanoes in
32 Azerbaijan, e.g. the Kotyrdag mud volcano. These models considering eruption dynamics
33 provide semi-quantitative support to purely conceptual formation models based on seismic
34 interpretation of subvolcanic stratal geometry.

35

36 **Plain language Summary**

37 We propose an initiation and early evolution model of an active mud volcano based on
38 previous observations, laboratory measurements and coupled numerical models. We built the
39 model upon our previous geological and geophysical interpretation of the Absheron mud volcano
40 in the South Caspian Basin, adding laboratory measurements on geological samples from the
41 mud volcano and its subsurface strata. New laboratory experiments indicate that gas bubble
42 growth in porous sediment disaggregates it into homogeneous mud. Our modeling of subsurface
43 pressure and fluid circulation evolution indicates that the presence of natural flow baffles is
44 paramount to generate mud below the mud volcano through bubble growth. Another model
45 based on fluid mechanics evaluated the impact of bubble growth on mud density and simulated
46 mud ascent to the seafloor. It suggests that eruption would happen 100 years after mud
47 generation at depth, a velocity similar to those measured on onshore mud volcanoes expelling
48 viscous mud. The new formation model integrates basin-scale fluid flow and eruption dynamics
49 and quantifies physical parameters required to trigger and sustain mud volcano formation.

50 **1. Introduction**

51 While extensive work has focused for decades on mud volcano (MV) architecture and on
52 gassy sediment structure and behavior, few studies have numerically explored MV formation and
53 evolution. Several authors have attempted to reproduce, through analogue models, field as well
54 as subsurface observations and suspected morphological evolution of MVs (Dupuis, 2017;
55 Mourgues et al., 2012; Nermoen et al., 2010; Odonne et al., 2020; Woolsey et al., 1975). The
56 results provide understanding of the evolution of surface structures and morphology as well as
57 exploring possible subsurface mechanisms responsible for the observed data. However, most of
58 these models used non-cohesive materials to simulate fine-grained cohesive sediments (Dupuis,
59 2017; Nermoen et al., 2010; Woolsey et al., 1975), following the theory on scaled models
60 (Hubbert, 1937). The processes used to remobilize material in the models may be different from
61 those applying to natural MVs. Other authors developed numerical models to explain the
62 subsurface mechanism and simulate the remobilization of mud (Brown, 1990; Collignon et al.,
63 2018a; Gisler, 2009; Zoporowski & Miller, 2009). These models are based on physical, chemical
64 and mechanical laws applied to natural conditions, therefore approaching processes more
65 accurately. However, these numerical models only assess the flow of fluid mud or the
66 mechanical evolution of mud during its ascent. Deville et al. (2010) computed regional fluid flow
67 models in the Barbados prism and showed that MVs are located above overpressured zones.
68 Therefore, modeling of mud volcanoes focused on reproducing the observed structures or the
69 mud flow dynamics, while other studies looked into the regional background to explain MV
70 location. To our knowledge, none of the previous models integrated both the regional and local
71 processes into a unique model. The impact of gas exsolution and expansion on subsurface
72 sediment mobilization has been inferred from geophysical observations (Brown, 1990; Imbert et
73 al., 2014; Lafuerza et al., 2012; Lawrence & Cartwright, 2010; Riboulot et al., 2013), but the
74 physics of gas-related mud generation commonly ignored or simplified.

75 The AMV has been densely surveyed for hydrocarbon exploration purposes and for
76 geohazard assessment (Contet & Unterseh, 2015; Dupuis, 2017; Gautherot et al., 2015; Unterseh
77 & Contet, 2015) giving a dense and high-quality multidisciplinary dataset. The SCB is also
78 densely studied, and several basin modeling integrating subsidence, thermal regime and
79 petrophysical properties of formations to reconstruct fluid flow over geological time provide
80 understanding of regional scale phenomena (Bredhoeft et al., 1988; Deville et al., 2010;
81 Grosjean et al., 2009; Javanshir et al., 2015). Overall, existing data present a unique opportunity
82 to model and simulate the formation of a mud volcano within its geological background.
83 Previous modeling work carried out by Blouin et al. (2019a) aimed to explain the location of the
84 AMV at the crest of the Absheron anticline, coupling sedimentation-related overpressure
85 generation and 2D-diffusion equations for fluid flow and methane diffusion. It showed that the
86 AMV was formed at the location where critical overpressure (near-fracture conditions) affected
87 methane-saturated areas. However, hydrofracturing conditions were not reached solely through
88 sedimentation and with the considered geological structure.

89 The present work assesses the following and complementary main questions:

- 90
- 91 • Is it possible to simulate mud generation conditions at depth by considering
92 mechanical properties of sediments, sedimentation rates, structural elements and
93 the impact of gas exsolution?
 - 94 • Is the sole impact of gas expansion on the mud properties able to drive mud up
to the seafloor?

95 Hereafter, we present the improvements brought to the 2D-diffusion model presented by
96 Blouin et al. (2019a) by considering a low-permeability interval corresponding to the Anhydritic
97 Surakhany Formation and by integrating fracture generation conditions, gas exsolution and
98 sediment damage (Blouin et al., 2019b) ; these make it possible to propose a possible geological
99 and physical setting and a chain of processes leading to mud generation. Modified Navier-Stokes
100 equations accounting for gas bubble expansion and changes in mud properties (density and
101 pressure) were used in order to simulate mud ascension through the sedimentary strata.

102 **2. Material and methods**

103 In addition to published data, we constrained the models using information from two
104 exploration wells (pressure, stratigraphy) and subsurface geometry from the interpretation of a
105 3D seismic volume (Blouin et al., 2019a) and using laboratory testing results showing the impact
106 of gas exsolution on the mechanical properties of compacted sediments (Blouin, et al., 2019b).

107 **2.1. Mud generation**

108 The method used to characterize sediment properties (including compressibility and
109 hydraulic conductivities) of the modelled stratigraphic layers was already discussed in the
110 companion paper (Blouin et al., 2019a). The software used to calculate the sedimentation-related
111 overpressure (SeCoV3 Ifremer in-house software) is also described (Blouin et al., 2019a) and no
112 further developments were done in the following modeling work.

113 The geometrical model, based on work by Green et al. (2009), was slightly modified
114 (Figure 1) to take into account the Anhydritic Surakhany Formation (ASF, Blouin et al., 2019a).
115 The fault network geometry is based on seismic interpretation (Blouin et al., 2019a).

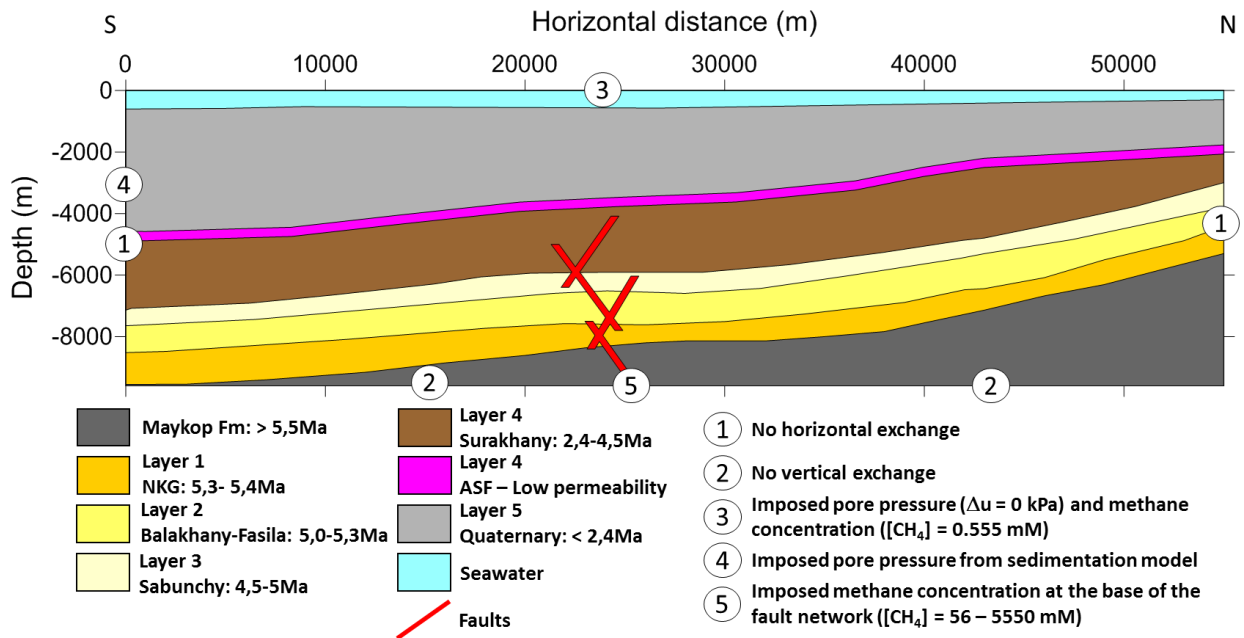
116 The 2D-diffusion method was modified from the initial version described in the
117 companion paper (Blouin et al., 2019a) in order to consider two additional phenomena:
118 hydrofracturing and gas compressibility and exsolution (Boyle's and Henry's laws). In a context
119 where the maximum principal effective stress is vertical ($\sigma'_1 = \sigma'_v$), hydrofracturing is vertical
120 and occurs when and where the fluid pressure exceeds the sum of the tensile strength of the host
121 sediment and the minimum horizontal stress (σ_3). For the purpose of modeling, a realistic
122 approximation is to consider that hydrofracturing occurs for a given ratio between overpressure
123 and vertical effective stress ($\Delta u/\sigma'_v$), generally obtained from pressure logs (see Blouin et al.,
124 2019a). When the ratio $\Delta u/\sigma'_v$ reaches this critical condition, hydrofractures are generated in the
125 concerned area. As a working hypothesis, the hydrofractured area permeability is calculated from
126 hydraulic conductivity laws (equation (2) in Blouin et al., 2019a) using a void ratio of 1.
127 Methane diffusivity in the hydrofractured area is considered as being the same as in faults.
128 Fracturing may trigger a decrease of overpressure in the fractured zone leading to a decrease in
129 the saturation concentration and consequently to gas exsolution. Hence, the degree of gas
130 saturation (S_g) after exsolution is calculated in the fractured area. The calculation follows
131 Boyle's law (methane compressibility) and the dissolution/exsolution capacity of methane
132 Henry's law (dissolution/exsolution capacity of methane), both being pressure and temperature
133 dependent. Therefore, temperature distribution was calculated over the modeled sedimentary
134 column. We estimated a thermal gradient from temperature measurements in the two exploration
135 wells (16°C/km; Blouin et al., 2019a) and seafloor temperature from Diaconescu et al., (2001) at
136 5.85°C.

137 Several studies noted that during marine sediment sampling, the structure and mechanical
 138 properties of sediments are impacted by gas exsolution and expansion (DeGroot et al., 2010;
 139 Esrig & Kirby, 1977; Priest et al., 2014; Sultan et al., 2010, 2012). Sultan et al., (2012)
 140 determined that damage of sediments from the Gulf of Guinea through a decrease in
 141 preconsolidation pressure was directly linked to the degree of gas saturation. This decrease in
 142 preconsolidation pressure with increasing degree of gas saturation was already highlighted on
 143 other sediments by several studies (Hight et al., 2002; Lunne et al., 2001). Blouin et al. (2019b)
 144 observed the same behavior on sediments from the Absheron mud volcano, mud being generated
 145 for a degree of gas saturation of 38 %.

146 The degree of gas saturation is consequently used to calculate the impact of gas
 147 exsolution on sediment damage through the equation obtained from laboratory testing on the
 148 AMV sediments (Blouin, et al., 2019b):

$$149 \quad \frac{\sigma'_{p2}}{\sigma'_{p0}} = \exp(-0.07 \cdot S_{gmax}) \quad (1)$$

150 with σ'_{p2} the preconsolidation pressure of sediments calculated after gas exsolution, σ'_{p0} the
 151 preconsolidation pressure of sediments before gas exsolution corresponding to the maximum
 152 vertical effective stress reached by the tested sample and S_{gmax} the maximum degree of gas
 153 saturation of the tested sample. Further details are available in Blouin et al. (2019b).



154
 155 Figure 1: Updated geometry considering the ASF as a 300-meter-thick incompressible and low-permeability layer (purple). The
 156 limit conditions are similar to the model presented in the companion paper (Blouin et al., 2019a). However, condition 5
 157 controlling the methane concentration injected at the base of the fault network is now considered as variable.

158 Methane and pore-pressure diffusion calculations may be initiated simulation stages
 159 accounting for hydrocarbon generation from mature source rocks since the beginning of Pliocene
 160 times, at the very beginning of the modeled sedimentation process. Boundary conditions are the
 161 same as those described and used in the companion paper (Blouin et al., 2019a) except for
 162 condition 5: the methane concentration imposed at the base of the fault network was considered
 163 between 56 and 5550 mM (Figure 1). In order to optimize the calculation time, the spatial

164 resolution was reduced by considering a vertical resolution of 192 m with a total of 50 vertical
165 nodes, and a horizontal resolution of 244 m with a total of 225 horizontal nodes (Figure 1).

166 Several tests were run on the hydraulic diffusivity (D_h) of the fault network, considering
167 faults as either transmissive or sealing for lateral fluid flow based on regional studies and
168 previous models (Battani et al., 2010; Bredehoeft et al., 1988; Caine et al., 1996; Evans et
169 al., 1997; Gautherot et al., 2015; Gordon & Flemings, 1998; Javanshir et al., 2015; Wibberley et
170 al., 2017).

171 **2.2. Mud ascent**

172 The numerical mud generation model is complemented by the modeling of the ascent of
173 the fluid mud. The purpose of this model is to determine whether the mud mass is able to rise up
174 to the seafloor through gas expansion processes only.

175 In order to model the mud flowing towards the surface, a fluid mechanics approach is
176 commonly adopted using simplified Navier-Stokes equations (Collignon et al., 2018a; Gisler,
177 2009; Zoporowski & Miller, 2009).

178 In this work, we used the Tryggvason et al. (2006) model by including the effect of free
179 gas expansion on the mud mass-density. More precisely, the software used in this paper is based
180 on code1 of Tryggvason (2012). The code is freely available and free of use (Tryggvason, 2011).
181 Navier-Stokes equations are governed by two basic equations. First, neglecting surface tension,
182 taking gravity as sole body force and assuming constant and uniform viscosity, the momentum
183 equation is given by Tryggvason et al. (2006) as:

$$184 \quad \rho \frac{\partial \mathbf{u}}{\partial t} + \rho \nabla \cdot \mathbf{u} \mathbf{u} = -\nabla p + \rho \mathbf{g} + \mu_0 \nabla^2 \mathbf{u} \quad (2)$$

185 where ρ is the mass-density of the mud (kg/m^3), \mathbf{u} is the fluid velocity (m/s), \mathbf{g} is the gravitational
186 acceleration (m/s^2), μ_0 is the viscosity considered as constant and uniform (Pa.s) and p is the
187 fluid pressure (Pa) (Tryggvason et al., 2006).

188 Secondly, mass conservation for incompressible fluids is given by:

$$189 \quad \nabla \cdot \mathbf{u} = 0 \quad (3)$$

190 as stated in Tryggvason et al. (2006).

191 One method for the resolution of this system of equations (Eq. (2) and Eq. (3)) is given
192 by Tryggvason (2012). The momentum equation is integrated with time by splitting Eq. (2) into
193 a velocity term and a pressure term, integrated separately. Then, each term of Eq. (2) is
194 discretized using a Finite-Volume approach where both equations are applied over a small
195 control volume. More details concerning the basic Navier-Stokes equations and the numerical
196 methods are provided in Tryggvason (2012).

197 In the present work, we introduce the effect of gas on the mud mass-density through the
198 following equation:

$$199 \quad \rho = \phi(1 - S_g)\rho_w + (1 - \phi)\rho_s \quad (4)$$

200 Where ϕ is the porosity and ρ , ρ_w and ρ_s are the respective mass-densities of mud, water and
201 solid particles. The density of free gas is considered as being negligible compared to the water
202 mass-density and the mass-density of the solid particles. Gas solubility and compressibility are

203 also calculated at each time step using Boyle's and Henry's laws.

204 We combined two approaches to model the ascent of low-density mud: one solving the
205 problem in two dimensions at low viscosities (Tryggvason, 2012) and one for extrapolating the
206 results to realistic higher viscosities using one-dimensional calculations (Furbish, 1997). The 2D
207 calculations were completed using the Datarmor Ifremer supercomputer (PCDM, 2018) allowing
208 to reduce significantly the time of calculation by parallel processing. Simulations that would
209 need a week on a PC could be completed on less than 24 hours using the Datarmor
210 supercomputer.

211 The 2D approach considers the mud as a one-phase fluid, whose flow was modeled using
212 simplified Navier-Stokes equations (Eq. (2) and Eq. (3)), deriving gas compressibility from
213 Boyles's law. Methane modifies the mass-density of the mud following Eq. (4) leading to mass-
214 density inversion between the mud generation zone and the host rock (Brown, 1990; Collignon et
215 al., 2018a; Deville, 2009; Kopf, 2002). Mud and host rocks are modelled as having the same
216 viscosity, constant over time and that does not vary with the presence of free gas. The resolution
217 method, using a discretization of the different terms of the simplified Navier-Stokes equations,
218 was adapted from Tryggvason et al. (2011).

219 Two modified versions of code1 were tested. The modifications were made at Ifremer,
220 for the purpose of the study. The first version (code1 v1) applies directly the numerical
221 resolution method of Tryggvason (2012) by considering gas exsolution and expansion
222 phenomena and by including in the computation the impact of free gas on the mass-density
223 evolution. The second version (code1 v2) considers an initial mud overpressure due to the
224 presence of free gas, which varies with the gas expansion during mud ascent.

225 The 2D simulation of mud ascent was completed over structural models with 100 x 100
226 nodes representing a 10-km-long and 4-km-thick section, corresponding to the approximate
227 length of the Absheron anticline in a SSW-NNE direction and to the depth below sea level of the
228 mud generation zone. The water column is considered and serves as an upper boundary limit
229 where no exchange with the mud and sediment zones is allowed. Therefore, the extrusion of mud
230 and its behavior after reaching the surface is not considered in the present work as it implies
231 complex chemical and physical interactions between sea water and formation water (Etiopie et
232 al., 2009; Kopf, 2002). The two lateral boundaries are considered as no-exchange boundaries.
233 The mass-density of the sediment decreases upward from 2100 kg/m³ at the base of the model to
234 1900 kg/m³ at the seabed. These values are calculated from porosities at wells, derived from
235 sonic data (equation (3) in Blouin et al., 2019a) and using a grain solid mass-density of 2650
236 kg/m³. An initial mud body is considered at the initial state corresponding to the volume of
237 damaged sediments calculated from the regional diffusion simulation and having the same mass-
238 density as unconsolidated marine sediments (1900 kg/m³). In code1 v2, this initial volume of
239 mud has also an initial overpressure which was obtained from diffusion simulations.

240 The mud generation process involves the formation of hydrofractures. These
241 hydrofractures should propagate vertically in the context of the extrados of the Absheron
242 anticline where normal faulting was observed. Therefore, vertical conduits having the same
243 mass-density as the mud source can be introduced in the initial geometry in order to simulate the
244 potential presence of vertical fractures.

245 Viscosities measured for surface marine sediments highly depends on the type of

246 sediments, but are clearly below 10^5 kPa.s (Jeong, 2013; Locat & Demers, 2008; Torrance,
 247 2010). However, this range of values is not representative of highly consolidated and stratified
 248 sediments, whose typical values of viscosity exceed 10^{14} kPa.s, value corresponding to
 249 evaporitic sediments (Collignon et al., 2018a; Mukherjee et al., 2010). With the depth range and
 250 type of host sediment encountered here, taking realistic values would have led to exceedingly
 251 long computation times. The Lusi catastrophe provided the first direct monitoring of a mud
 252 volcano initiation (Mazzini et al., 2012; Tingay et al., 2017; Tingay et al., 2015). Tingay et al.
 253 (2017) proved using the BJP-1 well data and reports that the mud generation and its ascent from
 254 a depth of 1000 m happened within two days. Following these observations, we limited the
 255 simulations to the first 24 hours after the mud generation, leading to calculations time on the
 256 Datarmor supercomputer of more than 30 days for a viscosity of 10^7 kPa.s. This directly arises
 257 from the resolution method: the time increment depends on the mesh resolution and on the
 258 viscosity. For instance, for a viscosity of 10^7 kPa.s and for the used mesh of 100×100 nodes
 259 (mesh resolution of 100 m horizontally and 39 m vertically), a time increment dt of 10^{-5} s was
 260 needed in order to reach numerical convergence. This implies 1.7×10^9 calculations to simulate
 261 the 24 hours of mud ascent. We therefore ran models based on Tryggvason (2012) over three
 262 orders of magnitudes for viscosity (10^5 , 10^6 and 10^7 kPa.s) and observed that the main change
 263 was with the timing, other parameters of interest being insensitive to viscosity changes.

264 The extrapolation to more realistic viscosity values was completed by a simple 1D
 265 calculation following a simple example of Furbish (1997) modeling a buoyant magma flow
 266 within a vertical dyke. It was possible to calculate the velocity of the ascending mud using the
 267 equation:

$$268 \quad v(x) = \frac{1}{2\mu}(\rho_c - \rho)g(r^2 - x^2) \quad (5)$$

269 with v the velocity of the ascending mud (m/s), μ the viscosity of the mud (kPa.s), ρ and ρ_c being
 270 the respective mass-densities of the mud and of the surrounding rock (reference) (kg/m^3), g the
 271 acceleration of gravity (m/s^2), r the radius of the mud chamber (m) and x the position relative to
 272 the center of the mud chamber (m). The mass-density of the reference rock was calculated just
 273 above the mud generation zone using the porosity obtained through the 2D sedimentation models
 274 and a mass-density for solid grains of 2650 kg/m^3 . The degree of gas saturation was taken at
 275 38 %, i.e. the limit for mud generation based on the laboratory testing by Blouin et al., (2019b).
 276 It allowed the calculation of the mud mass-density using Eq. (4). Therefore, applying Eq. (5), a
 277 maximum mud velocity was calculated for different sediment viscosities.

278 **3. Results**

279 **3.1. Mud generation**

280 **3.1.1. One-dimensional sedimentation and pore pressure accumulation**

281 The ASF is a 300-m-thick interval forming the uppermost interval of the Productive
 282 Series. It is comprised of a succession of evaporite beds and low resistivity shale intervals, some
 283 of which presented swelling behavior during drilling operations (Blouin et al., 2019a). It acts as
 284 an efficient seal, as overpressure rapidly builds up below this interval (Blouin et al., 2019a). The
 285 layer is therefore modeled as being incompressible ($C_C = 0$) and with a permeability reduced by
 286 one to two orders of magnitudes compared to other layers, and three orders of magnitude lower

287 than the most permeable layer (Layer 4). Its sedimentation rate was taken equal to the one used
288 for Layer 4, as being part of the same overall stratigraphic interval.

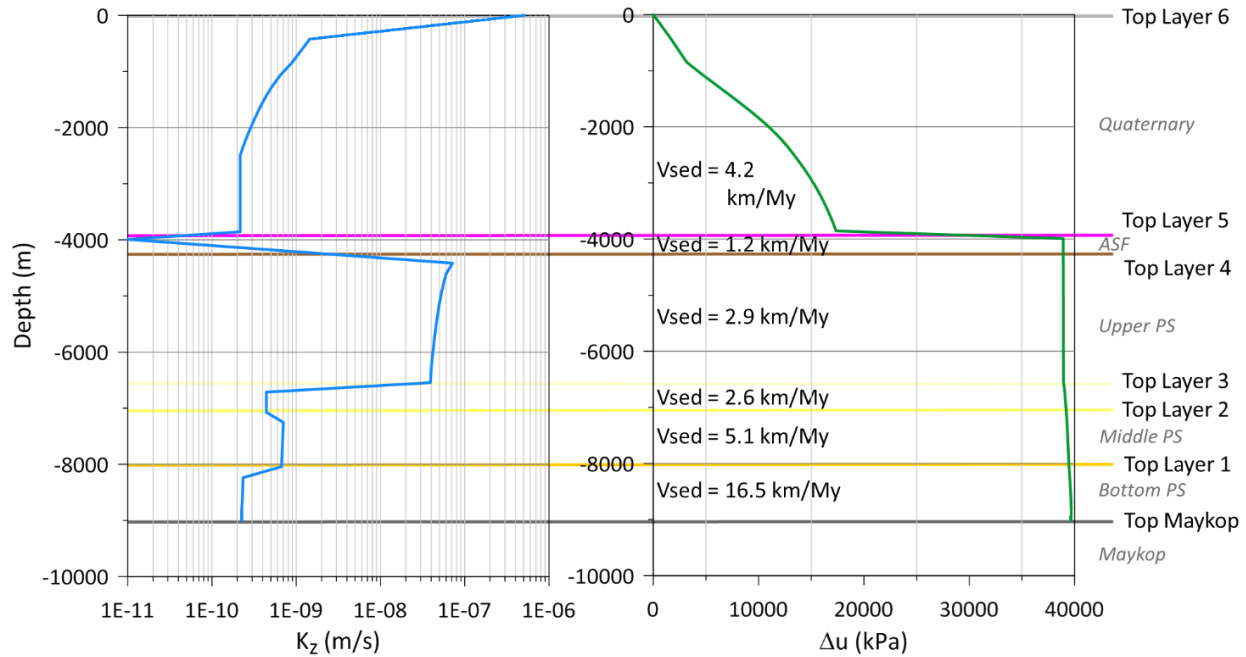
289 The presence of the low permeability ASF has prevented fluids from being expelled
290 during the burial of the Productive Series. The increase in the overpressure gradient below the
291 ASF described in the companion paper (Blouin et al., 2019a) clearly shows that fluids are
292 trapped below the ASF, building-up the overpressure in the underlying strata. Therefore, the
293 Upper PS might have kept an abnormally high porosity through compaction disequilibrium
294 (Osborne & Swarbrick, 1997). Pressure data reported in Javanshir et al. (2015) as well as the
295 reservoir overpressure values detailed in the companion paper (Blouin et al., 2019a) show that
296 the Middle Productive Series and Lower Productive Series are drained through laterally
297 continuous and connected reservoirs, which should have limited under-compaction in these
298 intervals. Thus, in the following simulations Layer 4 permeability was artificially kept higher
299 than in underlying and overlying intervals using a modified permeability law (Eq. (6)). That
300 modified law reproduces the under-compaction caused by the ASF as displayed in Figure 2:

$$301 \quad \ln(K) = 3.06 e - 17.66 \quad (6)$$

302 with K the hydraulic conductivity in m/s, and e the void ratio.

303 Using permeabilities obtained from oedometer tests and well data analysis (Blouin et
304 al., 2019a), initial 1D properties were obtained from the deeper part of the section presented in
305 Figure 1. We ran 13 iterations to estimate compaction-corrected deposition rates from the
306 observed present-day thicknesses. The corrected sedimentation rates are summarized in Figure 2
307 and are quite similar to those obtained in the previous modeling work presented in the
308 companion paper (figure 10 in Blouin et al., 2019a).

309 Figure 2 displays the main results of the 1D modeling that are taken as boundary
310 condition 4 (Figure 1) in the 2D-diffusion models presented below. The results show the impact
311 of the low-permeability ASF on overpressure that rises sharply when crossing this interval,
312 accounting for the observed pressure build-up in well pressure logs (Blouin et al., 2019a). The
313 low-permeability zone is well expressed in Figure 2 and contrasts with the high-permeability
314 Layer 4. The overpressure slowly builds up over Layer 1, stays constant over Layer 4 and
315 slightly increases over Layer 3, 2 and 1. The highest overpressure reached 40 MPa, which is in
316 accordance with the pore pressure measured in the wells (Blouin et al., 2019a).



317
 318 Figure 2: Results of the one-dimensional sedimentation modeling at the southern edge of the 2D geometrical model in Figure 1.
 319 On the left, vertical hydraulic conductivity versus depth trend at the end of the 5 My of sedimentation. On the right, overpressure
 320 versus depth trend at the end of the 5 My of sedimentation with corrected sedimentation rates for each layer. The top of each
 321 simulated stratigraphic unit is represented as indication using the same color code as in Figure 1 and the corresponding
 322 stratigraphic intervals are displayed in between.

3.1.2. Two-dimensional transient-diffusion processes, gas exsolution and damage

324 Four numerical simulations were conducted with different input parameters. The
 325 parameters used during the simulations are synthetized in Table 1. Most of the parameters are
 326 common for all the simulations and were obtained from literature and industrial reports (seafloor
 327 temperature, Henry methane constant) or from laboratory testing and well log interpretation
 328 (temperature gradient, sediment petrophysical properties; Blouin et al., 2019a). Four parameters
 329 were modified in order to fit observations and regional geology: fault hydraulic diffusivity,
 330 fracture condition, starting date for overpressure transmission, initial methane concentration.

331 Table 1: Parameters used for the different diffusion simulations presented in this study. Several parameters were modified to fit
 332 observations and regional background over the different simulations. e_0 is the initial void ratio, C_c is the compression index, T
 333 the temperature, K is the hydraulic conductivity (K_h in the horizontal direction, K_v in the vertical direction), D_h is the hydraulic
 334 diffusivity, D_c the methane molecular diffusivity, Δu is the overpressure, σ'_v is the vertical effective stress and e_{frac} the fracture
 335 void ratio.

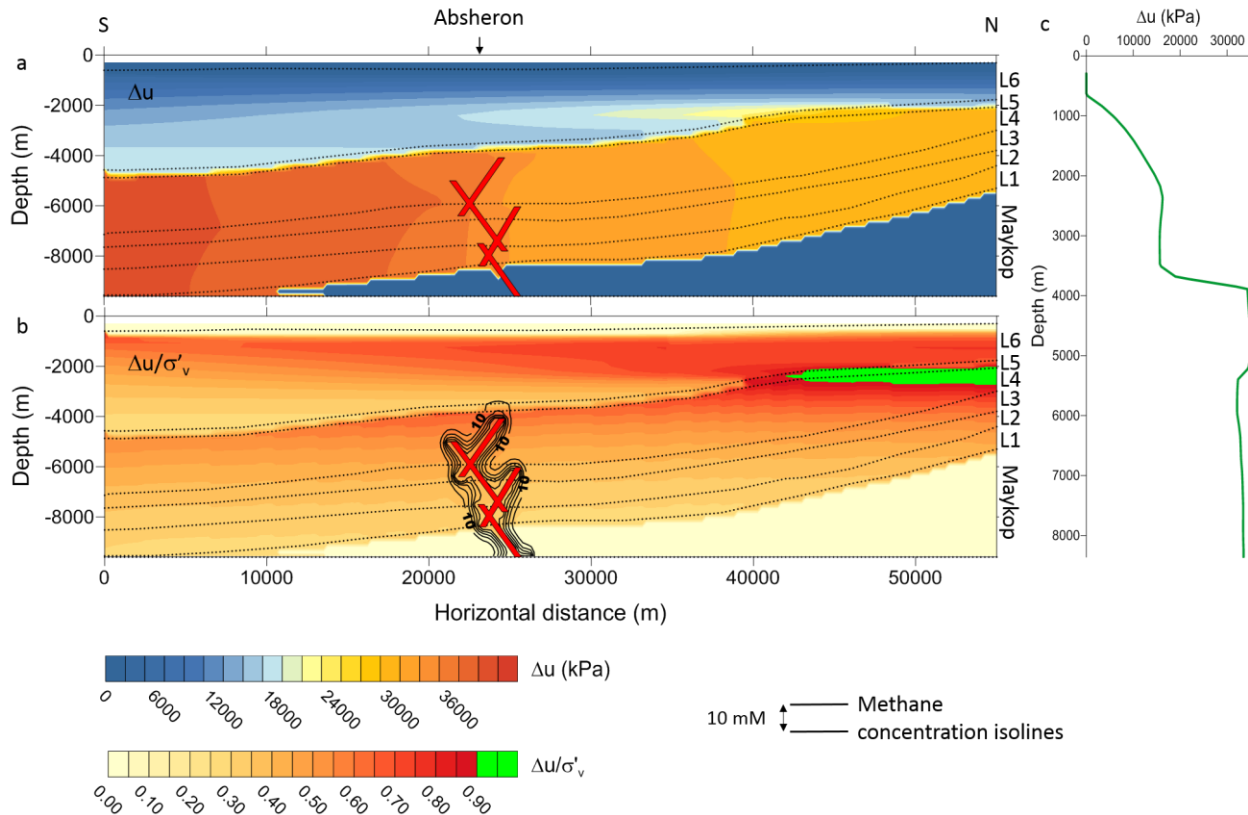
| | | Simulation 1 | Simulation 2 | Simulation 3 | Simulation 4 |
|------------------------|--------------|--|--------------|--------------|--------------|
| nodes number | vertically | 50 | | | |
| | horizontally | 225 | | | |
| Seafloor temperature | | 5.85°C | | | |
| grad(T) | | 16°C/km | | | |
| Henry methane constant | | $1.5 \times 10^{-3} \text{ M.atm}^{-1}$ | | | |
| fluid viscosity | | $1.15 \times 10^{-6} \text{ kPa.s}$ | | | |
| methane diffusivity | | $1.49 \times 10^{-7} \text{ m}^2/\text{s}$ | | | |
| e_0, C_c | Layer 6 | 2.734; 0.159 | | | |
| | Layer 5, ASF | 0.500; 0.000 | | | |

| | | | | | |
|--|--------------|--|----------------------|----------------------|----------------------|
| | Layer 4 | 2.014; 0.105 | | | |
| | Layer 3 | 1.821; 0.094 | | | |
| | Layer 2 | 1.643; 0.080 | | | |
| | Layer 1 | 1.659; 0.081 | | | |
| a, b, K_h/K_v $K=\exp(ae+b)$ (m/s) | Layer 6 | 3.064; -22.866; 2200.0 | | | |
| | Layer 5, ASF | 0.000; -25.328; 15.0 | | | |
| | Layer 4 | 3.064; -17.666; 15.0 | | | |
| | Layer 3 | 3.064; -22.150; 5.0 | | | |
| | Layer 2 | 3.064; -21.803; 2.0 | | | |
| | Layer 1 | 3.064; -22.333; 1.0 | | | |
| e_0, C_c | faults | 3.5; 0.0 | | | |
| D_h (m ² /s) | | 5.5×10^{-6} | 5.5×10^{-8} | 5.5×10^{-8} | 5.5×10^{-8} |
| D_c (m ² /s) | | 5.5×10^{-6} m ² /s | | | |
| fracture condition: $\Delta u/\sigma'_v$ | | 0.9 | 0.9 | 0.7 | 0.7 |
| e_{frac} | 1.0 | | | | |
| Start of overpressure diffusion (Ma) | 1 My | 1 My | 1 My | 3 My | |
| Initial methane concentration (mM) | 55.5 | 55.5 | 55.5 | 5550 | |

336 i. Case 1: integration of the ASF layer properties

337 The 2D geometrical model, based on the work presented in Green et al. (2009), was
 338 modified in order to consider the impact of the low permeability of the ASF. The modeled
 339 geometry is displayed in Figure 1. The fracture condition $\Delta u/\sigma'_v$ was initially set at 0.9 given the
 340 mean fracture condition obtained from well data (Blouin et al., 2019a). Lateral overpressure
 341 transmission started 1 My after inception of methane diffusion in fault networks. Results of this
 342 simulation after 5 My are displayed in Figure 3. Methane diffusivity was set at 1.49×10^{-7} m²/s
 343 in sediments, and faults have a hydraulic diffusivity of 5.5×10^{-6} m²/s and a relatively high
 344 methane diffusivity coefficient of 5×10^{-4} m²/s in order to artificially include gas advection
 345 impact and create a preferential advective pathway for fluids.

346 Figure 3a shows overpressure diffusion across the structural model. Overpressure
 347 strongly increases below the ASF, reaching 38 MPa in the south of the model, and stays lower
 348 than 18 MPa above the ASF. Moreover, as Layer 4 is more permeable than the others,
 349 overpressure propagates more rapidly along this stratigraphic layer. Figure 3c shows the
 350 overpressure build-up below the ASF at the Absheron location that reaches 35 MPa over less
 351 than 1000 m. The main difference with results obtained without the ASF (figure 12 in Blouin et
 352 al., 2019a) is this clear and strong pressure build-up in Layer 4. The previous simulation
 353 calculated higher overpressure in Layer 5 (corresponding to Layer 6 in this paper), and
 354 overpressure increase with depth was more progressive.



355

356 Figure 3: Results of overpressure and methane diffusion modeling after 5 My of calculation considering the low permeability
 357 ASF interval. Black dotted lines are for layer limits. Layer names are reported at the right of the sections. a: overpressure (Δu) in
 358 kPa after 5 My of migration through the structural model presented on Figure 1. Overpressure migrated more rapidly through
 359 layer 4 that has a higher permeability. b: $\Delta u/\sigma'_v$ contours with values exceeding hydrofracture condition below the ASF in the
 360 north of the model, where σ'_v is low. Black lines correspond to methane concentration contours. Lines are separated by 10 mM.
 361 c: Δu (kPa) vertical plot at the Absheron location (black arrow).

362 However, in terms of $\Delta u/\sigma'_v$ distribution, Figure 3b clearly shows that the maximum is
 363 reached just below the ASF, in the northern edge of the model where σ'_v is low due to thin
 364 overburden and probably to the boundary condition (Figure 1), which prevents lateral exchanges
 365 between the model and the outsides, therefore allowing overpressure build-up along the northern
 366 edge of the model. Hydrofracturing conditions are reached as $\Delta u/\sigma'_v$ is above 0.9 (green area in
 367 Figure 3b). No fracture conditions are reached at the Absheron location where calculated values
 368 do not exceed 0.7. Methane circulation is effective around the fault network showing that over
 369 5 My, sediments get saturated with dissolved methane through the simulated transmissive fault
 370 network. The values of $\Delta u/\sigma'_v$ calculated here are higher than in the simulations described in the
 371 companion paper (figure 12 in Blouin et al., 2019a). The highest values are now localized below
 372 the ASF (Figure 3b) when they were distributed along the interval immediately above in the
 373 former version of the simulation (figure 12 in Blouin et al., 2019a). Methane distribution is
 374 similar to that of the former simulation (figure 12 in Blouin et al., 2019a) as the parameters for
 375 methane diffusivity were not modified.

376 Thus, the presence of the low permeability ASF allows reproducing pressure transmission
 377 and build-up mainly below this interval as well as reaching hydrofracturing conditions along the
 378 bottom end of the ASF. However, fractures open at the northern end of the structural model

379 where σ'_v is lowest and where overpressure accumulates due to model boundary effects. Besides,
380 no free gas, and consequently no sediment damage was observed due to fracture formation in an
381 area where no dissolved gas was present.

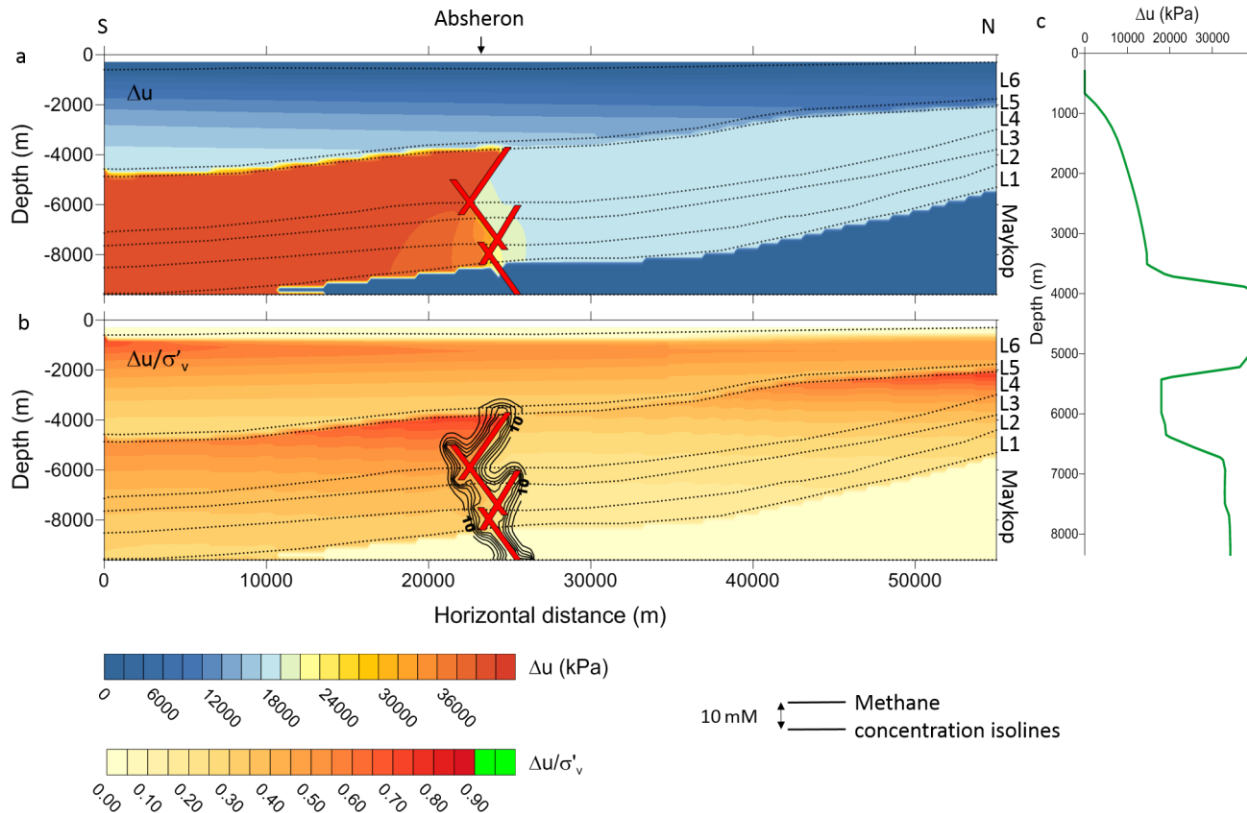
382 **ii. Case 2: sealing faults**

383 The previous simulation shows that overpressure does not accumulate at the Absheron
384 location but at the northern boundary of the model. Therefore, another simulation was conducted
385 with modified boundary conditions. The pore pressure was drained at several levels below the
386 ASF in order to dissipate overpressures in the north by setting Δu to zero. Hinds et al. (2004) and
387 Javanshir et al. (2015) show that several sandstone intervals of the Productive Series are
388 continuous and crop out onshore, especially in the lower PS. Therefore, the modeled hydraulic
389 connection between the deeper part of the SCB and the surface, where atmospheric pressure
390 prevails, does exist and was directly inferred from pressure logs at different well sites (Blouin et
391 al., 2019a; Javanshir et al., 2015). However, the results of the simulation were inconclusive as
392 overpressure was entirely dissipated at the north border of the model without any hydrofracturing
393 in the calculation zone. Besides, the $\Delta u/\sigma'_v$ at the Absheron location did not change.

394 Thus, another working hypothesis was tested. Faults were initially set to create
395 preferential pathways for fluids. Nevertheless, faults could be vertical pathways but horizontal
396 seals for fluid circulation due to permeability anisotropy (Caine et al., 1996; Evans et al., 1997;
397 Wibberley et al., 2008). Indeed, different authors noted in several regions around the world that
398 faults may be sealing in the perpendicular direction but transmissive along the fault direction and
399 that their permeability may vary depending on external parameters such as pore pressure,
400 deformation style and the lithologies put in contact through the fault and within the fault itself
401 (Henry et al., 2019; Morley et al., 2017; Wibberley et al., 2017). This feature was also already
402 highlighted over the SCB and particularly in the Absheron anticline where gas was found in the
403 northern flank while no economic gas accumulation was encountered in the southern flank
404 (Gautherot et al., 2015; Grosjean et al., 2009; Javanshir et al., 2015). Several regional fluid flow
405 numerical models already integrated fault anisotropy (Deville et al., 2010; Gordon & Flemings,
406 1998; Schneider et al., 2004). Besides, now that the ASF is modeled, slight corrections in the
407 fault geometry are needed to fit the observations of the companion paper where the fault network
408 ends in the ASF (figure 4 in Blouin et al., 2019a).

409 To simulate the horizontal sealing effect of the fault, the hydraulic diffusivity of the fault
410 was taken equal to 5.5×10^{-8} m²/s. Vertical transmissivity was simulated by keeping a methane
411 diffusivity of 5×10^{-4} m²/s. Results of this simulation are displayed in Figure 4.

412 Figure 4a displays the 2D distribution of overpressure after 5 My of calculation. The
413 main feature is that with the sealing faults, overpressure builds up south of the faults, reaching 40
414 MPa, while in the northern part, the overpressure stays limited (around 18 MPa). The effect of
415 the high permeability layer 4 contrasting with the low permeability ASF is still displayed with
416 overpressure transmitting more rapidly along Layer 4 than in overlying intervals and with limited
417 overpressure buildup in Layer 1. Figure 4c shows the overpressure profile with depth at the
418 Absheron location. The sharp overpressure increase across the ASF and the weak overpressure
419 gradient along Layer 1 are well captured by the model. Besides, an overpressure contrast is
420 visible between Layer 4 and Layer 3 due to the effect of sealing faults, creating a trend similar to
421 that observed in pressure logs at wells, with pressure horns and peaks (Blouin et al., 2019a).



422

423

424

425

426

427

428

Figure 4: Results of overpressure and methane diffusion modeling after 5 My of calculation considering the low permeability ASF interval and faults as horizontal seals. Black dotted lines are for layer limits. Layer names are reported at the right of the sections. a: overpressure (Δu) in kPa after 5 My of migration through the structural model presented on Figure 1. Overpressure builds up along the fault network. North of the fault network overpressure is only of 18 MPa. b: $\Delta u/\sigma'_v$ contours. The highest values are now distributed south of the fault network, along the ASF, at the crest of the Absheron fold. Methane distribution is represented with black isolines, lines being separated by 10 mM. c: Δu (kPa) vertical plot at the Absheron location (black arrow).

429

430

431

432

433

434

435

436

High values of $\Delta u/\sigma'_v$ are now distributed in two main areas. To the north of the structural model where σ'_v is low and where some overpressure accumulated below the ASF, but most of all just south of the sealed fault network and along the ASF at the crest and along the southern flank of the Absheron anticline (Figure 4b). However, the fracture condition 0.9 is not reached, thus no fractures were created. The highest $\Delta u/\sigma'_v$ values reached are comprised between 0.70 and 0.75 (Figure 4b). Methane diffusion is similar to what was observed in the previous simulations as methane diffusivity of faults and sediments were not modified (Figure 4b). Methane concentrations are also the same.

437

438

Therefore, the fault network now acts as a seal for lateral pressure transmission and as a vertical pathway for fluids, allowing to approach critical conditions at the Absheron location.

439

iii. Case3: new assessment of fracture conditions

440

441

442

443

444

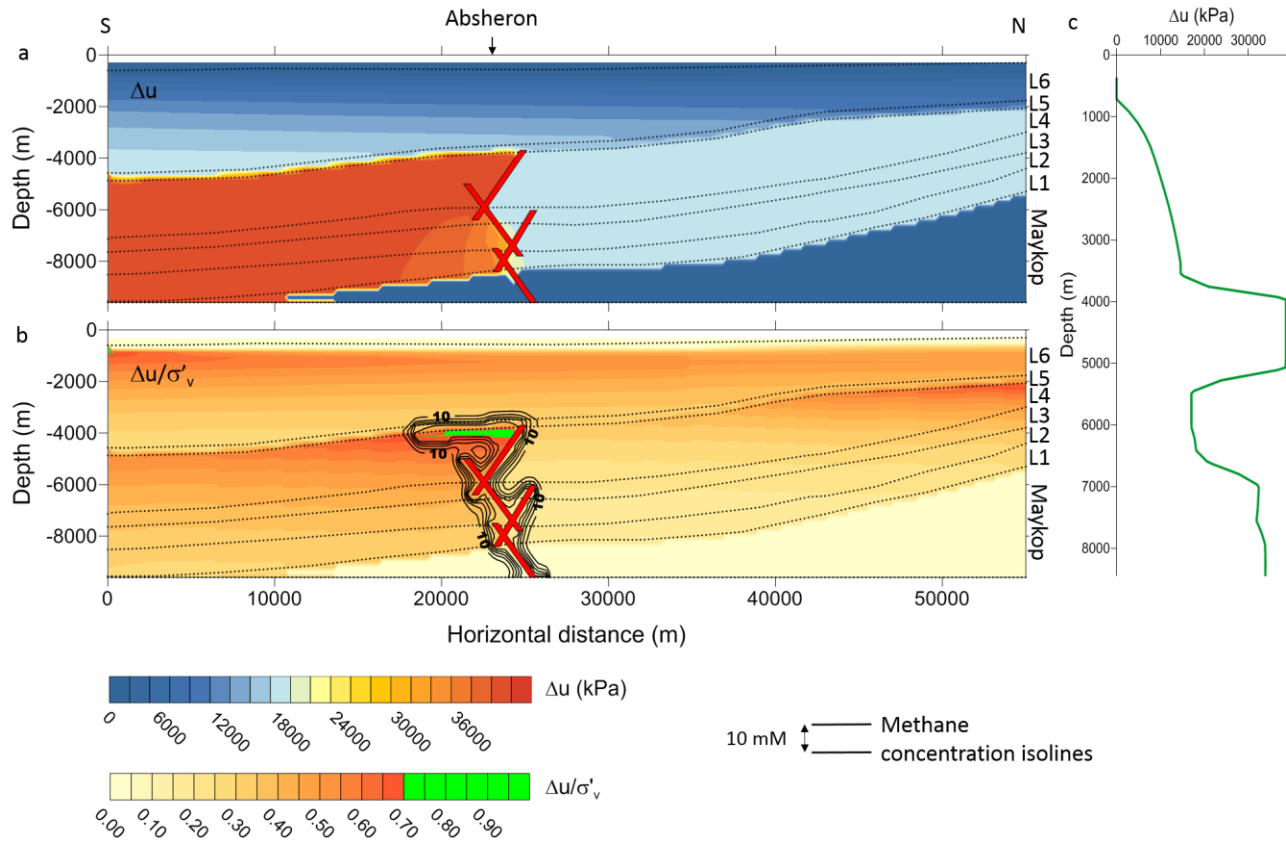
The fracture condition was previously set at 0.9 because of the mean value obtained on well data of the ratio between fracture pressure and overburden pressure. However, this value may be as low as 0.8 depending on the considered depth. Besides, at the time when the AMV started being active, sediments may have been less consolidated than at present which led to lower tensile strength hence lower hydrofracturing conditions. Therefore, a fracture condition of

445 0.7 was considered as plausible and is now considered in the following calculations. This value
446 $\Delta u/\sigma'_v$ was already given as a minimum value for brittle failure of sedimentary rocks in several
447 studies (Grauls & Baleix, 1994; Sibson, 2003).

448 A new calculation only changing the critical fracture criterion from 0.9 to 0.7 was carried
449 out. Figure 5 synthesizes the results after 5 My of calculation.

450 Figure 5a and Figure 5c are roughly the same as Figure 4, as no changes were made that
451 could affect directly the pressure field. Figure 5b shows that fracture condition was reached and
452 that a fracture opened in the area of the Absheron anticline, south of the fault network, where
453 $\Delta u/\sigma'_v$ is the highest. As fractures have a methane diffusivity of $5 \times 10^{-4} \text{ m}^2/\text{s}$, pore fluids
454 migrated through the fractures along a horizontal plane, changing the distribution of the
455 concentration of dissolved methane (Figure 5b). However, no gas exsolution occurred in this
456 model, since the degree of gas saturation stayed at zero. This could be either due to the fact that
457 the pressure drop through fracture was not high enough, or that the dissolved methane
458 concentration is not sufficient, two parameters that control gas exsolution processes (Brown,
459 1990; Duan & Mao, 2006). Figure 5a and Figure 5c do not display any pressure decrease at
460 fracture depth. As fractures are generated in an area where overpressure is constant, no drainage
461 of fluids was possible, preventing pore pressure from a significant decrease. A vertical fracture
462 that would have connected Layer 4 and Layer 6 through the ASF would have permitted a strong
463 pressure decrease. Nevertheless, this was not possible since the ASF layer is characterized by a
464 low-permeability coefficient impeding vertical pore pressure diffusion and therefore
465 hydrofracturing.

466 Another important point is that hydrofracturing happened only 500,000 years after the
467 beginning of pressure diffusion calculation, so 1.5 My after the beginning of the simulation. This
468 shows that there is no need for calculating diffusion for a period as long as 5 My and that
469 diffusion calculation could start at 3 Ma, date when all the PS were already deposited (Abreu &
470 Nummedal, 2007; Forte & Cowgill, 2013; Green et al., 2009; Morton et al., 2003; Vincent et al.,
471 2010). This could account for the deposition time of the main reservoirs, when hydrocarbon
472 generation was already active (Guliyev et al., 2011; Inan et al., 2002; Smith-Rouch, 2006;
473 Tagiyev et al., 1997).



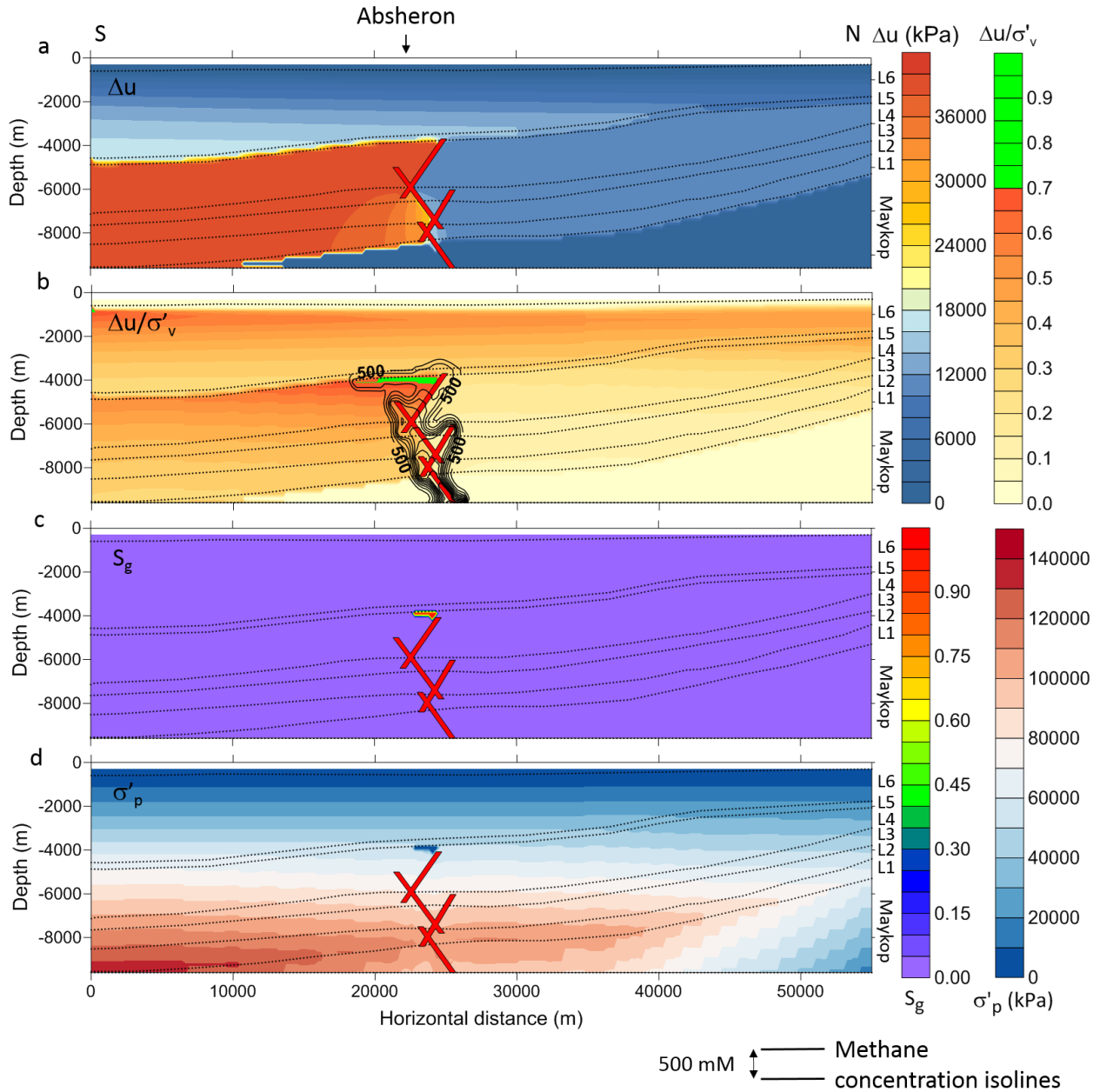
474

475 Figure 5: Results of overpressure and methane diffusion modeling after 5 My of calculation considering the low permeability
 476 ASF interval, faults as horizontal seals and a fracture condition of 0.7. Black dotted lines are for layer limits. Layer names are
 477 reported at the right of the sections. a: overpressure (Δu) in kPa after 5 My of migration through the structural model presented on
 478 Figure 1. b: $\Delta u/\sigma'_v$ contours. Fracture occurs along the bottom edge of the ASF, south of the fault network. Methane distribution
 479 is represented with black isolines, lines being separated by 10 mM. The dissolved methane distribution follows the fracture
 480 shape. c: Δu (kPa) vertical plot at the Absheron location (black arrow).

481 As a conclusion of this calculation, fractures were generated at the Absheron anticline
 482 crest, south of the fault network, and dissolved gas diffused into the fracture network. However,
 483 no free gas was formed because of either unsubstantial pressure decrease or low dissolved
 484 methane concentration.

485 **iv. Case 4: high gas concentration at the base of the fault network**

486 In order to test the impact of free gas at the fracture location (Figure 5b), the dissolved
 487 methane concentration of the fluid source at the bottom of the fault network (coming from a
 488 deeper source such as the Maykop source rock) was increased to 555 mM and to 5550 mM. The
 489 latter high methane concentration (twice higher than methane solubility at the entry point
 490 temperature and pressure conditions) imply the presence of free gas in addition to dissolved
 491 methane. However, this initial free gas volume which accumulates during several thousands of
 492 years, during sedimentation processes, is not supposed to cause any damage to the sediment as it
 493 would get dissolved as overburden increases. Here, damaging is considered to occur only during
 494 short-term exsolution process. The simulations start calculating pressure diffusion after 3 My of
 495 methane diffusion through the faults and the stratified sediment layers.



496

497 Figure 6: Results of the simulation considering the ASF, sealing faults, a fracture condition of 0.7 and an initial methane
 498 concentration of 5550 mM after 5 My. Black dotted lines are for layer limits. Layer names are reported at the right of the
 499 sections. a: overpressure (Δu) in kPa after 2 My of migration through the structural model presented on Figure 1. b: $\Delta u / \sigma'_v$
 500 contours. Fracture occurs along the bottom edge of the ASF, south of the fault network. Methane distribution is represented with
 501 black isolines. The dissolved methane distribution follows the fracture shape and is depleted around fractures due to gas
 502 exsolution. c: degree of gas saturation (S_g) calculated after fracture formation. Values as high as 1 are reached in the central part
 503 of the fracture, in an area close to the fault network. d: preconsolidation pressure (σ'_p). It increases linearly with depth, but it is
 504 disturbed in the same area where gas exsolution happened reaching zero in the center of the fracture.

505 The simulation considering an initial methane concentration of 555 mM was not
 506 conclusive as the results obtained are the same in Figure 5. However, this showed that pore-
 507 pressure diffusion starting at 3 My does not impact the previous results.

508 Figure 6 shows the results of the simulation with an initial methane concentration of

509 5550 mM. Figure 6a shows that the overpressure field does not change compared to previous
510 simulations. Figure 6b shows a similar $\Delta u/\sigma'_v$ distribution than in Figure 6b with a fracture
511 generation below the ASF, south of the fault networks. The dissolved methane concentration
512 follows faults and fractures but with higher concentrations, the lower value plotted being
513 500 mM (Figure 6b). Figure 6c displays the degree of free gas saturation (S_g) calculated across
514 the structural model. S_g is above zero in an area corresponding to the fractured area close to the
515 fault network and just below the ASF limit. Maximum values of 1 are reached in the center of
516 the fractures. The model triggers gas exsolution locally after fracture generation for sufficient
517 dissolved methane concentration.

518 Gas exsolution has a twofold effect. First, dissolved methane distribution is disturbed and
519 partly depleted around the faults compared to the simulation proposed in Figure 5 (see Figure 6b)
520 due to the fact that, locally, a part of the initially dissolved methane exsolved to form free gas.
521 Moreover, as the simulation calculates the preconsolidation pressure (σ'_p), based on Eq. (1)
522 (Blouin et al., 2019b) linking S_g with a preconsolidation ratio, we observe a local decrease in
523 preconsolidation pressure in response to the presence of free methane (Figure 6d). This decrease
524 in σ'_p is observed in the area where S_g is non-zero. σ'_p reaches almost 0 kPa where S_g is greater
525 than 0.38, in areas where it was around 50 MPa before gas exsolution (Figure 6d).

526 Thus, this simulation considering 1- the presence of the ASF; 2- sealing faults; 3- a
527 fracture condition of 0.7; and 4- an initial methane concentration of 5550 mM, was able to model
528 sediment damage in an area just below the ASF and at the Absheron anticline crest, through
529 fracture opening and the subsequent gas exsolution.

530 The integration of a low permeability layer corresponding to the ASF allowed
531 transmitting overpressure into the Upper Productive Series and reaching critical overpressure
532 conditions. The modification of fault hydraulic diffusivity in order to create horizontal seals
533 resulted in critical conditions at the crest of the Absheron Anticline. These critical conditions
534 created fractures that, coupled with sufficiently high dissolved methane concentration, allowed
535 gas exsolution. Gas exsolution locally decreased the preconsolidation pressure of sediments
536 sufficiently for them to lose all their initial structure. The observations made during the
537 laboratory testing led by Blouin et al. (2019b) allow concluding that with the parameters used,
538 conditions for mud generation are reached in the Upper Productive Series, at the Absheron mud
539 volcano location.

540 **3.2. Mud ascent**

541 The approximate volume of mud and the initial geometrical conditions for mud ascent
542 modeling were estimated from the previous calculations of the mud generation (Figure 6). The
543 initial (2D) mud body for all simulations was set as a convex-up half-disc with a radius of 500 m,
544 its base (diameter of the half-disc) being located 3400 m below seafloor with 500 m of water
545 column above and centered on the horizontal axis of the model (Table 2). For code1 v2, the
546 initial mud overpressure was set at 35 MPa, which is the pressure obtained in the mud generation
547 zone at the end of the simulation presented in Figure 6. Mass-densities used for all simulations
548 are indicated in Table 2.

549 Three values of the common viscosity of the ascending mud and host sediments were
550 tested using both codes (with and without pressurized mud) as well as the impact of the presence
551 of vertical conduits and of their length (Table 2).

552
553

Table 2: Parameters used in the different simulations completed during the study. The varying parameters are the sole sediment viscosity and the fracture length.

| code version | viscosity (kPa.s) | conduit length (m) | dimensions | | mud source | | | Mass-densities (kg/m ³) | | | |
|--------------|-------------------|--------------------|------------|-----------|--------------|--------------------------|---------------------|-------------------------------------|------|------|--------------|
| | | | length | depth | dimension | position | overpressure | bottom | top | mud | Solid grains |
| code1 v1 | 10 ⁵ | 0 | 10 km | 3900 m | radius 500 m | x = 5000 m z = 3900 m | No mud overpressure | 2100 | 1900 | 1900 | 2650 |
| | | 1000 | | | | | | | | | |
| | | 2000 | | | | | | | | | |
| | 10 ⁶ | 0 | | | | | | | | | |
| | | 1000 | | | | | | | | | |
| | | 2000 | | | | | | | | | |
| | 10 ⁷ | 0 | | | | | | | | | |
| | | 1000 | | | | | | | | | |
| | | 2000 | | | | | | | | | |
| code1 v2 | 10 ⁵ | 0 | 100 nodes | 100 nodes | radius 500 m | x = 5000 m z = 3900 m | 35 MPa | 2100 | 1900 | 1900 | 2650 |
| | | 1000 | | | | | | | | | |
| | | 2000 | | | | | | | | | |
| | 10 ⁶ | 0 | | | | | | | | | |
| | | 1000 | | | | | | | | | |
| | | 2000 | | | | | | | | | |
| | 10 ⁷ | 0 | | | | | | | | | |
| | | 1000 | | | | | | | | | |
| | | 2000 | | | | | | | | | |

554

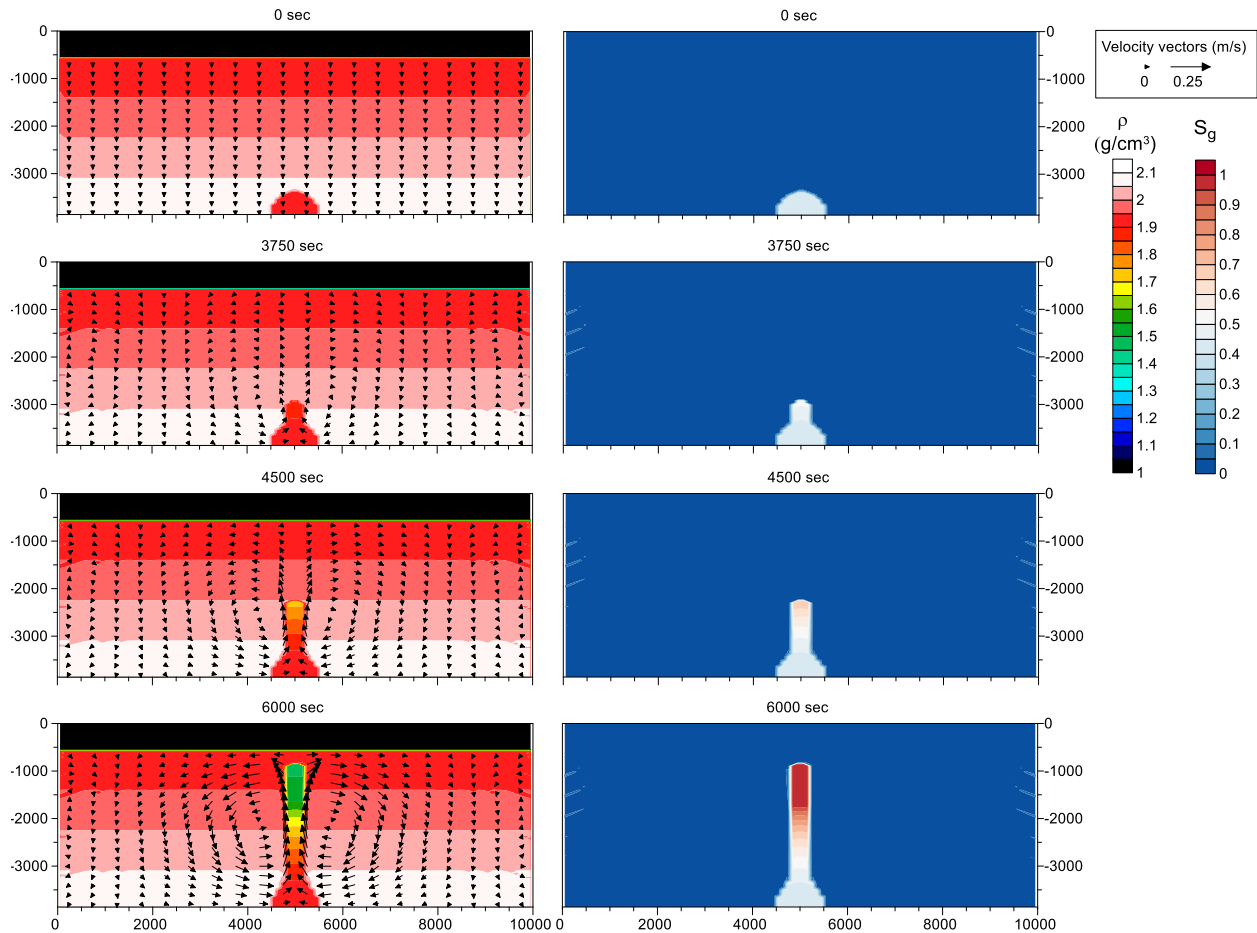
3.2.1. Code1 v1

555
556
557
558
559
560
561
562
563
564
565
566
567
568
569
570
571
572

Figure 7 displays the results of the simulation for the median case, $\mu = 10^6$ kPa.s, using code1 v1. The initial state shows the initial geometry of the mud generation zone modeled as a 500 meters radius half-disc. The imposed mass-density is displayed, varying linearly from 1900 kg/m³ at the seafloor to 2100 kg/m³ at 3900 m. The mud mass-density is initially at 1900 kg/m³. The degree of gas saturation (S_g) is initially 0 everywhere except in the mud generation zone where it is set at 0.38. The gassy-mud column starts rising after 3500 s. The changes in mass-density are mainly localized around the gassy-mud column and the velocity vectors are mainly disturbed in the immediate vicinity of the mud source reaching 0.04 m/s at 3750 s. The surrounding stratified sediments stay undisturbed, apart from the lateral edges where boundary conditions create some artifacts. As the degree of gas saturation increases due to methane expansion, the mass-density in the mud decreases (orange and green colors in Figure 8), triggering an acceleration of the process at 4500 s, when the gassy-mud column reaches 2200 m. The surrounding sediments are also impacted as the gassy-mud column rises, as non-negligible displacements are computed 2000 m away from the column with velocities reaching 0.1 m/s at 4500 s. The final stage (6000 s) shows that the gassy-mud column reaches the seafloor, with a width of 500 m. The corresponding mass-density of the gassy-mud column has values of 1450 kg/m³ just below the seafloor. The gassy mud displays velocities of 0.25 m/s and surrounding sediments are disturbed significantly up to 3000 m away from the center of the

573 model. The mass-density of the host sediment remains stable except near the model lateral
 574 boundaries due to computation artifacts. However, the initial stratification is preserved.

575 For $\mu = 10^5$ kPa.s (minimum case), the same observations are made but events occur
 576 10 times faster. The initiation of mud ascent is observed after 350 s, and the final stage is reached
 577 after only 600 s. The velocity reaches 3.2 m/s in the ascending column and displacements are
 578 also visible in a radius of 3000 m around the center of the model. The stratification is also
 579 preserved and the ascending column is nearly 1 km wide. The mass-density is not disturbed
 580 around the gassy-mud column.

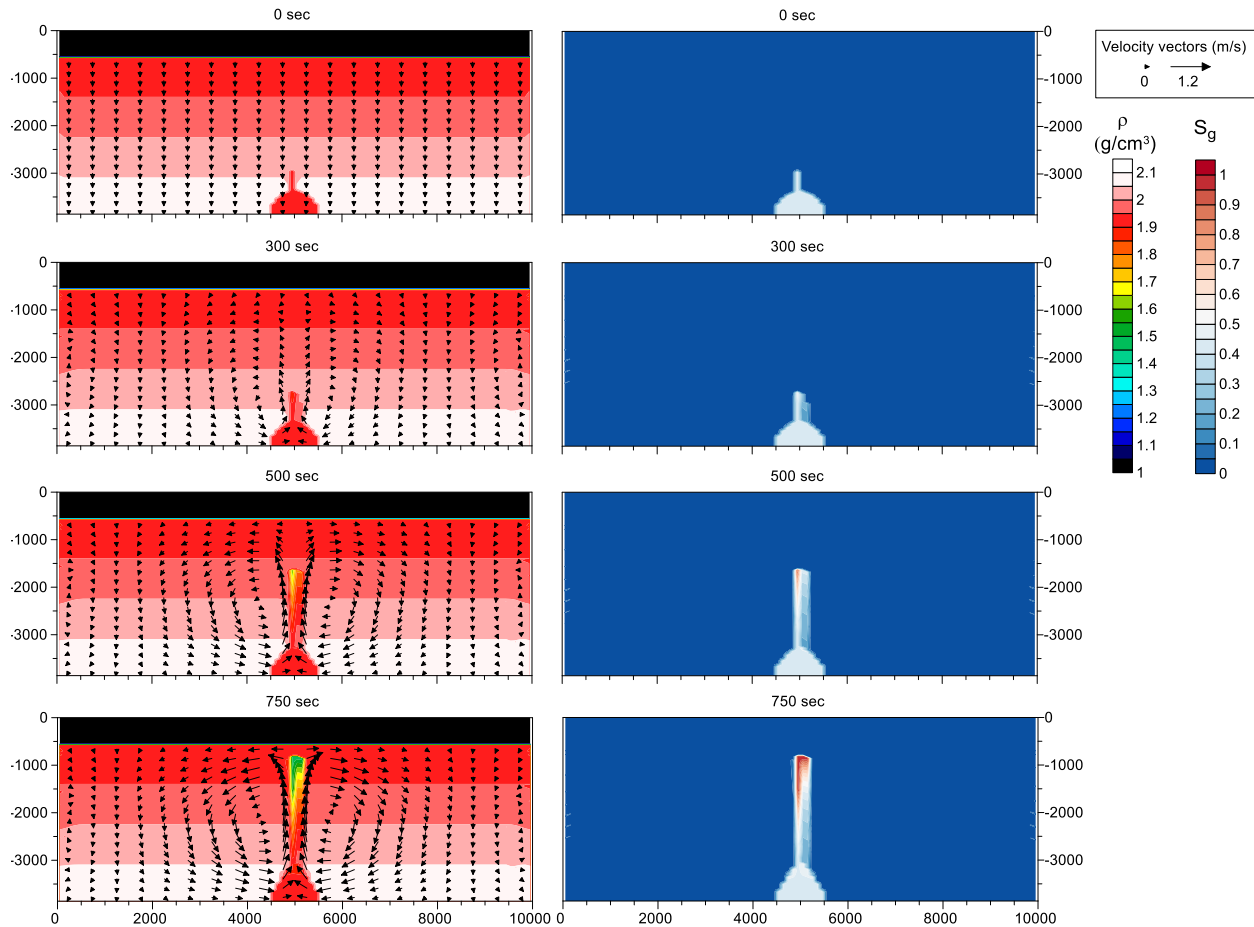


581
 582 Figure 7: Results of the simulation using code1 v1 for $\mu = 10^6$ kPa.s. The left column displays the evolution of mass-density with
 583 time (left color scale) as well as the velocity vectors (m/s). The right column displays the evolution of the degree of gas saturation
 584 with time (right color scale).

585 For $\mu = 10^7$ kPa.s (maximum case), after 100,000 s, the gassy sediment column does not
 586 rise. We therefore tested the response of the simulation when a pre-existing conduit was added to
 587 the model (Table 2). As there are 100 nodes horizontally, it was not possible to center the
 588 vertical conduit, hence creating some dissymmetry in the results of simulations presented
 589 hereafter.

590 Two conduit lengths were tested: 1000 m and 2000 m from the base of the model
 591 (Table 2). The result of the simulation with $\mu = 10^5$ kPa.s and a 1000 m long vertical conduit is
 592 presented in Figure 8, where the conduit is displayed at the initial stage, with the same mass-

593 density and the same degree of gas saturation as the mud generation zone. The initiation of
 594 gassy-mud ascent starts at 300 s. The gassy-mud ascent is mainly focused along the conduit, but
 595 it is superimposed with the normal gassy-mud ascent due to the presence of the mud source (as
 596 was observed without conduit). It is particularly visible as the conduit is not perfectly centered
 597 over the mud generation zone. The final stage is reached at 750 s. The final width of the gassy-
 598 mud column is 250 m. The velocity of the host sediments reaches 1.2 m/s at the direct proximity
 599 of the conduit and decreases to nil over a distance of 3 km. The timing of ascent conduit of 2-km
 600 conduit is very similar to the previous one, but the velocity only reaches 0.5 m/s, and the gassy-
 601 mud ascent is only focused above the vertical discontinuity, hence the final gassy-mud column is
 602 only 100 m wide.



603
 604 Figure 8: Results of the simulation using code1 v1 for $\mu = 10^5$ kPa.s and a 1000 m long vertical conduit. The left column displays
 605 the evolution of mass-density with time (left color scale) as well as the velocity vectors (m/s). The right column displays the
 606 evolution of the degree of gas saturation with time (right color scale).

607 We also tested the impact of conduits for $\mu = 10^6$ kPa.s. The results are overall similar to
 608 what has been described above with $\mu = 10^5$ kPa.s, apart from the timing: initiation of gassy-
 609 mud ascent happens after 3000 s for both conduit lengths, and mud reaches the seafloor after
 610 7000-7500 s. The maximum velocity is 0.12 m/s for a 1-km conduit and 0.05 m/s for a 2-km
 611 conduit. The width of the gassy-mud column remains unchanged.

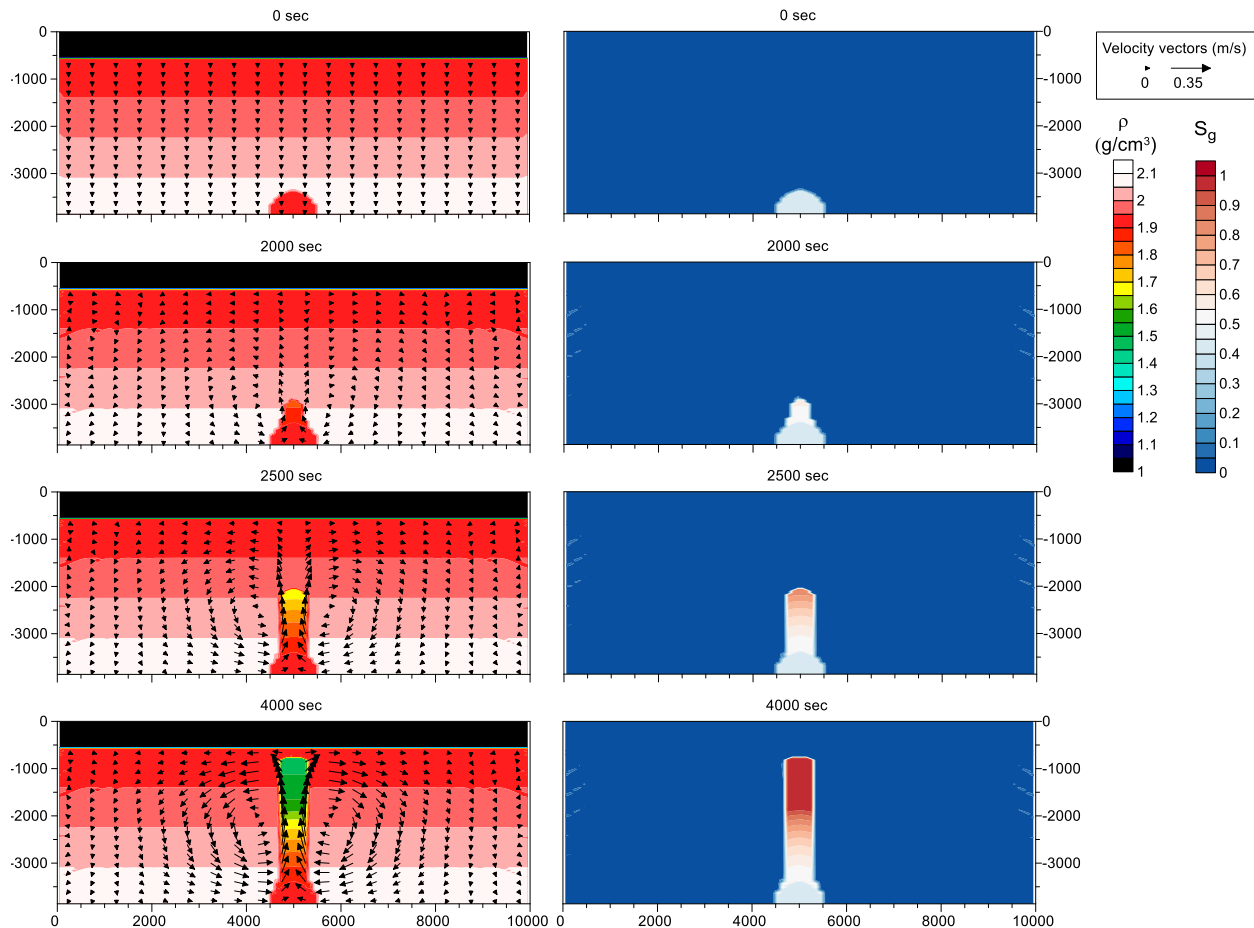
612 With $\mu = 10^7$ kPa.s, even with 2 km-long conduits, no gassy-mud column was observed,
 613 even after 100,000 s, corresponding to over 3 weeks of computation time, exceeding the time

614 limitation imposed on the Datarmor supercomputer.

615 3.2.2. Code1 v2

616 Code1 v2 considers the initial mud overpressure and its evolution with gas expansion.
617 Fluid pressure in Eq. (2) is calculated separately through Boyle's law when free gas is present.

618 Figure 9 displays the results of the simulation for $\mu = 10^6$ kPa.s using code1 v2. The
619 initial state is the same as in Figure 7. The different stages described for code1 v1 are the same
620 with this version, but they occur earlier in the simulation. The ascending column initiates at
621 1750 s, and it is accompanied by a slight disruption in velocity vectors as shown in Figure 9 at
622 2000 s. This disruption increases as the ascending gassy-mud column rises, reaching 0.35 m/s in
623 the ascending column at the final stage of the simulation and affecting a radius of 3000 m around
624 the center of the model. The ascending column reaches the seafloor after 4000 s. A minimum
625 mass-density of 1450 kg/m^3 is obtained at the top of the ascending column near the seafloor,
626 1000 m above the depth where the degree of gas saturation reaches 1. The ascending column is
627 nearly 750 m wide at the final stage. The initial mass-density stratification is preserved as in
628 Figure 7. Some computation artifacts due to the limit conditions of the model are still present.

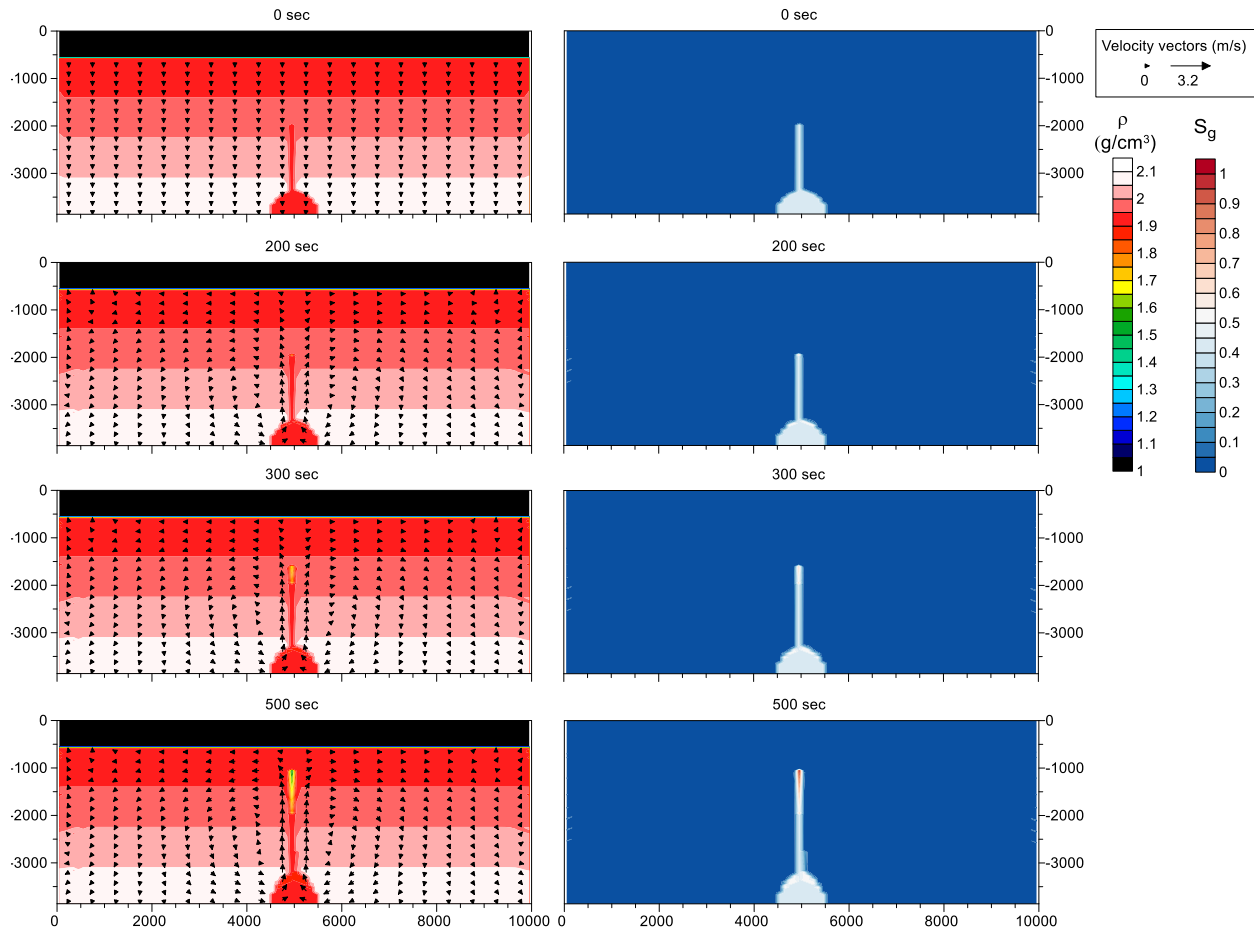


629
630 Figure 9: Results of the simulation using code1 v2 for $\mu = 10^6$ kPa.s. The left column displays the evolution of mass-density with
631 time (left color scale) as well as the velocity vectors (m/s). The right column displays the evolution of the degree of gas saturation
632 with time (right color scale).

633 Again, for $\mu = 10^5$ kPa.s the same observations are made but 10 times earlier in the

634 simulation than in Figure 9. The initiation of gassy-mud ascent is observed after 200 s, and the
 635 final stage is reached after only 400 s. The velocity reaches 3.5 m/s in the ascending column and
 636 displacements are also visible in a radius of 3000 m around the center of the model. The
 637 stratification is also preserved and the ascending column is also 750 m wide. The density is not
 638 disturbed near the column.

639 As observed earlier in code1 v1, for $\mu = 10^7$ kPa.s, after more than 10 days of
 640 computations, the simulation only reached 5000 s, and no initiation of an ascending column was
 641 visible. Further simulations with vertical discontinuities were made to understand the impact of
 642 conduits above the mud source (Table 2).



643
 644 Figure 10: Results of the simulation using code1 v1 for $\mu = 10^5$ kPa.s and a 2000 m long vertical conduit. The left column
 645 displays the evolution of mass-density with time (left color scale) as well as the velocity vectors (m/s). The right column displays
 646 the evolution of the degree of gas saturation with time (right color scale).

647 At $\mu = 10^5$ kPa.s, the presence of a 1 km long vertical discontinuity generates similar
 648 effects to those obtained with code1 v1 and displayed in Figure 8. The gassy-mud column
 649 initiates at 200 s, mainly focusing along the conduit, but the direct impact of the mud generation
 650 zone is also visible (same as Figure 8). The column reaches the seafloor after 400 s, reaching
 651 750 m in diameter and velocities of 4.2 m/s above the mud chamber. The velocity field is
 652 disturbed in a radius of 3 km around the conduit. The case of a 2-km conduit is displayed in
 653 Figure 10. An ascending gassy-mud column starts forming at 200 s just at the termination of the
 654 vertical conduit. The mud column gets larger at 300 s, forming a drop-shaped low-density area.

655 The gassy mud reaches the surface between 500 and 600 s with velocities reaching locally
 656 3.2 m/s at the intersection between the conduit and the mud chamber. The gassy-mud column is
 657 100 m wide at the end of the simulation.

658 This version of the code leads to computation times even longer than the first version, so
 659 no process initiation was observed for $\mu = 10^7$ kPa.s, even with 2 km-long conduits.

660 All the results obtained with the different 2D simulations discussed above are synthesized
 661 in Table 3. These results highly depend on the spatial and temporal resolution of the simulations,
 662 hence small variations are not considered to be relevant. It clearly shows that when viscosity
 663 increases by one order of magnitude, velocity decreases by one order of magnitude while the
 664 timing of initiation and extrusion increases by one order of magnitude (Table 3). When mud
 665 overpressure is considered in the simulations, it decreases the time for initiation and extrusion by
 666 a ratio of 0.65 to 0.5 (Table 3). The presence of vertical conduits above the mud chamber mainly
 667 influences the V_{\max} which seems to decrease as the length of the conduit increases in the case of
 668 code1 v1 (Table 3). For code1 v2, V_{\max} seems to remain roughly constant. The presence of a
 669 conduit also influences the final diameter of the gassy-mud column that decreases as the length
 670 of the conduit increases (Table 3).

671 Table 3: Synthesis of the main results obtained from the different simulations computed in this study. The initiation time of
 672 gassy-mud ascent, the time needed to reach the seafloor, the maximum velocity and the final diameter of the gassy-mud column
 673 are displayed for the two code versions.

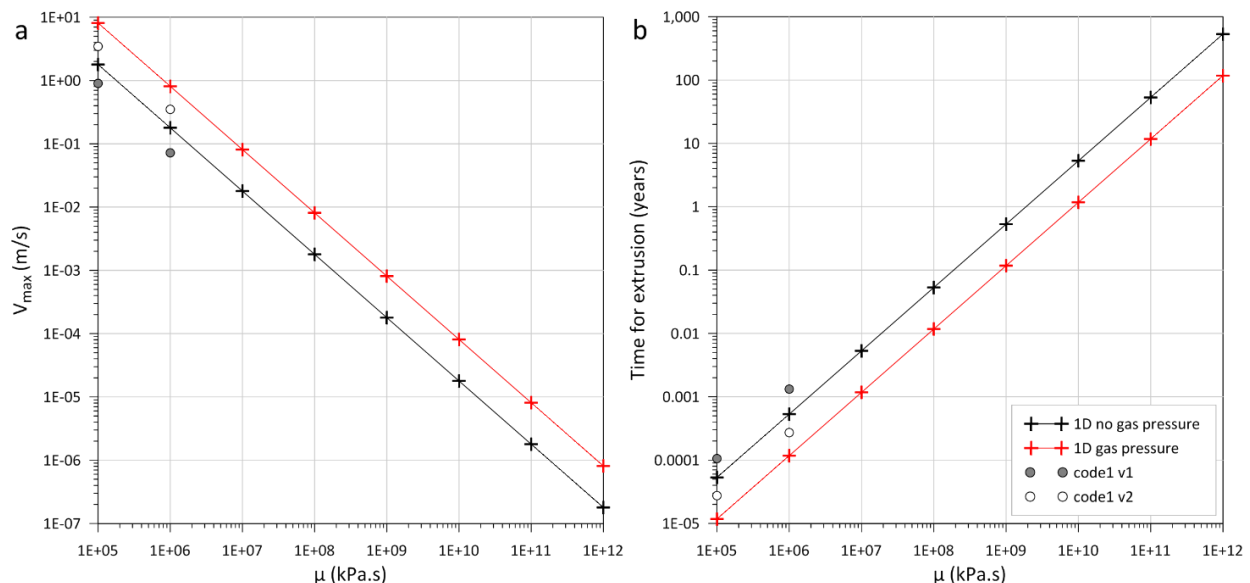
| code | μ (kPa.s) | Conduit length (m) | Initiation (s) | Extrusion (s) | Max. velocity (m/s) | Final diameter of gassy-mud column (m) |
|------|---------------|--------------------|--------------------------------|---------------|---------------------|--|
| 1 v1 | 10^5 | 0 | 350 | 600 | 3.2 | 1000 |
| | | 1000 | 300 | 750 | 1.2 | 250 |
| | | 2000 | 300 | 750 | 0.5 | 100 |
| | 10^6 | 0 | 3500 | 6000 | 0.25 | 500 |
| | | 1000 | 3000 | 7000 | 0.12 | 250 |
| | | 2000 | 3000 | 7500 | 0.05 | 100 |
| | 10^7 | 0 | Computation too time consuming | | | |
| | | 1000 | | | | |
| | | 2000 | | | | |
| 1 v2 | 10^5 | 0 | 200 | 400 | 3.5 | 750 |
| | | 1000 | 200 | 500 | 4.2 | 400 |
| | | 2000 | 200 | 500 | 3.2 | 100 |
| | 10^6 | 0 | 1750 | 4000 | 0.35 | 750 |
| | | 1000 | 1500 | 4500 | 0.36 | 400 |
| | | 2000 | 2000 | 4750 | 0.32 | 100 |
| | 10^7 | 0 | Computation too time consuming | | | |
| | | 1000 | | | | |
| | | 2000 | | | | |

674

3.2.3. Extrapolation to realistic viscosities: 1D calculations

675 In order to extrapolate the 2D simulation results obtained through the code modified from
 676 Tryggvason (2012), we tested simple 1D calculations based on the case of a buoyant magma
 677 flow along a vertical dyke (Furbish, 1997) in order to compare the velocities and timing
 678 obtained. Using Eq. (5) with r the radius of the mud chamber ($r = 500$ m) and taking $x = 0$
 679 (maximum velocity above the center of the mud chamber) it was possible to obtain the maximum
 680 velocity above the mud chamber for varying viscosities. Figure 11a shows the results of 1D
 681 calculations of maximum velocities (V_{\max}) for viscosities comprised between 10^5 and 10^{12}
 682 kPa.s, considered as a valid approximation range for mud viscosities that are typically below the
 683 viscosity of sedimentary rocks. Two sets of models were run: the first one without initial mud
 684 overpressure (black), corresponding to the mud mass-density calculated through Eq. (4); the
 685 second (red line) considers an initial mud overpressure. Overpressure is limited to 78% of the
 686 effective stress (value of $\Delta u/\sigma'_v$ near the mud source at the end of 2D diffusion models;
 687 Figure 6), thus, the mass-density of mud was multiplied by 0.78 to take the mud overpressure
 688 into account. The maximum velocities obtained above the mud chambers for the 2D simulations
 689 without conduit are also plotted in Figure 11a. Figure 11b displays the same results in terms of
 690 minimum time for extrusion that was calculated considering that the velocity is V_{\max} all along the
 691 conduit. The results in Figure 11b clearly show that the minimum time needed for the buoyant
 692 mud to reach the seafloor and form a mud volcano depends on mud viscosity.

693 One-dimension calculations show that the maximum velocity is inversely proportional to
 694 the viscosity (Figure 11a). Considering the initial mud overpressure, without modifying the
 695 viscosity, increases V_{\max} by a factor 4.5, so that the two trends are parallel. For higher viscosities
 696 (10^{12} kPa.s), the maximum velocity is comprised between 10^{-6} and 10^{-7} m/s. Logically, the
 697 time for extrusion increases by an order of magnitude for each order of magnitude of μ
 698 (Figure 11b), a result which directly arises from the form of Eq. (5). The consideration of the
 699 mud overpressure allows reducing this time for extrusion. Therefore, for $\mu = 10^{12}$ kPa.s, it would
 700 take a minimum of 500 years for the buoyant mud to reach the surface if mud overpressure was
 701 not considered, while it only takes 100 years if mud overpressure is integrated in the calculation.



702

703

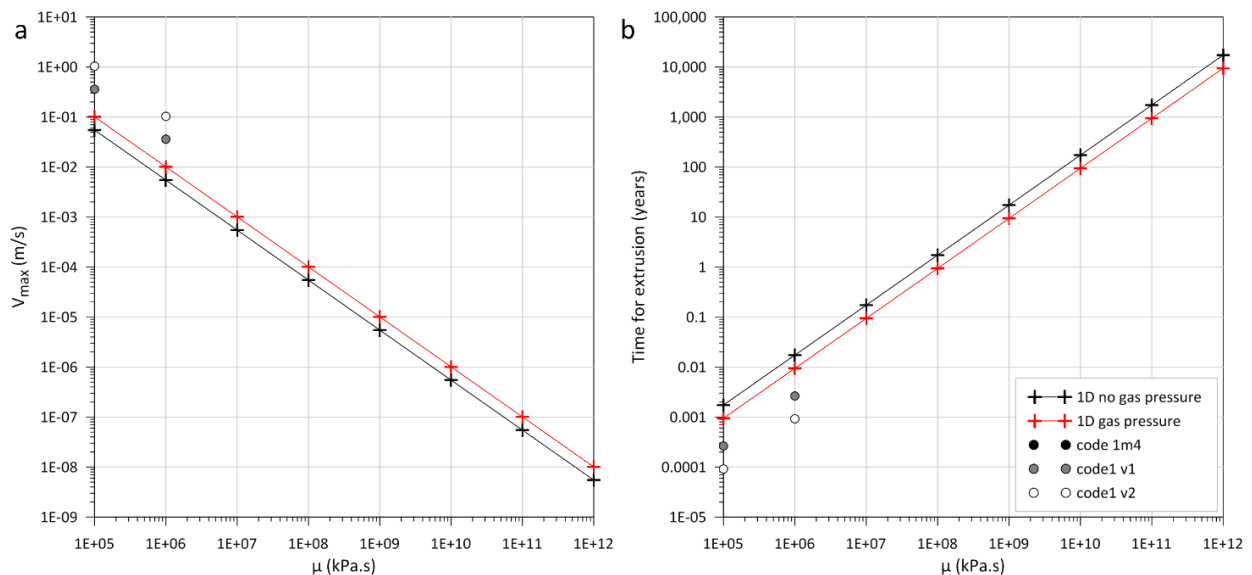
Figure 11: Results of 1D calculations based on the case of a buoyant magma flow along a vertical dyke presented in Furbish

704 (1997) considering a radius of 500 m corresponding to the mud source radius, compared to results obtained with 2D simulations.
 705 a: maximum velocity versus viscosity, b: minimum time for extrusion versus viscosity. Black lines with crosses correspond to the
 706 case where the initial mud overpressure is not considered, red lines are for the case with mud overpressure. Grey dots correspond
 707 to the results of the 2D simulations using code1 v1 and white dots the results of 2D simulations with code1 v2.

708 The 2D simulations results display the same relationship. μ and V_{\max} are inversely
 709 proportional (Figure 11a). Considering the initial mud overpressure in code1 v2 leads to a 4-fold
 710 increase of V_{\max} compared with code1 v1 (Figure 11a). Moreover, the values obtained with
 711 code1 v1 stands close to the black line (1D calculations without mud overpressure), and the
 712 values of code1 v2 are closer to the red line compared to code1 v1 results (1D calculations
 713 considering mud overpressure).

714 The same calculation was applied but in the case of a 50-m-wide conduit corresponding
 715 to the size of the conduits in the 2D simulations (Figure 12). The same relationship between μ
 716 and V_{\max} and μ and the time for extrusion are displayed in Figure 12. The impact of mud
 717 overpressure seems to be limited as the difference between the V_{\max} and the time for extrusion
 718 obtained considering mud overpressure and without mud overpressure is reduced compared to
 719 Figure 11. Moreover, V_{\max} values extracted from 2D simulations are larger by nearly one order
 720 of magnitude than those obtained from 1D calculations (Figure 12a). Therefore, the time for
 721 extrusion is smaller by one order of magnitude (Figure 12b). Besides, the conduit width
 722 corresponds to the minimum that could be computed considering the model resolution, one node
 723 corresponding to 100 m and the conduit being computed over a unique node. Hence, the results
 724 displayed are not representative of the circulation that would occur in natural fractures whose
 725 width is much smaller.

726 From this 1D calculation, it arises that the time required for achieving extrusion,
 727 considering a viscosity of 10^{12} kPa.s, is significantly increased. Considering mud overpressure,
 728 it would take more than 10,000 years for the mud to reach the surface through thin fractures
 729 when it was 100 years for the calculation considering the mud chamber radius.



730
 731 Figure 12: Results of 1D calculations based on the case of a buoyant magma flow along a vertical dyke presented in Furbish
 732 (1997) considering a radius of 50 m corresponding to the conduit width, compared to results obtained with 2D simulations. a:
 733 maximum velocity versus viscosity, b: time for extrusion versus viscosity. Black lines with crosses correspond to the case where
 734 the initial mud overpressure is not considered, red lines are for the case with mud overpressure. Grey dots correspond to the
 735 results of the 2D simulations using code1 v1 and white dots the results of 2D simulations with code1 v2.

736

4. Discussion

737

4.1. Synthesis of the main results

738

739

740

741

742

743

744

745

746

747

748

749

750

751

752

753

754

755

756

757

758

759

760

Representing the low-permeability Anhydritic Surakhany Formation (ASF) in the model generates a sedimentation-related overpressure contrast between layer 6 and deeper layers, thus reproducing the sharp overpressure increase observed in well-log data (Blouin et al., 2019a). Moreover, the model simulates maximum overpressure values of 40 MPa corresponding to the values measured in situ at the Absheron exploration wells (Blouin et al., 2019a). It also improved the preliminary 2D diffusion model presented in the companion paper (figure 12 in Blouin et al., 2019a) with overpressure now occurring essentially below the ASF and transmitted through Layer 4 (Figure 3). Overpressure diffusion started after 3 My of simulation, a duration corresponding to the deposition of the entire Productive Series interval. Lateral compartmentalization of the 2D model through the presence of faults having low horizontal permeability (Gautherot et al., 2015; Javanshir et al., 2015) was necessary to generate overpressure at the location of the AMV (Figure 4). Faults are commonly regarded as presenting permeability anisotropy, with the higher permeability along the fault surface (Caine et al., 1996; Deville et al., 2010; Evans et al., 1997; Henry et al., 2019; Morley et al., 2017; Schneider et al., 2004; Wibberley et al., 2008), thus methane-saturated water migration from the Maykop Fm. was provided by high methane diffusivity in faults, artificially simulating high vertical permeability accounting for advection processes. A new fracture condition of 0.7 based on pressure logs at well sites was adopted, which generated in the model a fractured area at the Absheron crest, just below the ASF (Figure 5). For an initial methane concentration of 5550 mM, gas exsolution was triggered in the fractured area resulting in a strong sediment damage in the fracture zone, with preconsolidation pressure locally approaching zero (Figure 6). From the results of the laboratory testing discussed by Blouin et al. (2019b) the improved 2D diffusion model simulated the mud generation zone formation below the Absheron MV.

761

762

763

764

765

766

767

768

769

770

771

772

773

774

775

776

777

778

779

780

To understand a possible ascent mechanism of the mud from its source to the seafloor, we based our approach on fluid mechanics using modified 2D Navier-Stokes equations considering the impact of gas expansion (Boyle's law) on the mass-density of the mud. Mud viscosities were limited to values between 10^5 kPa.s and 10^7 kPa.s because higher viscosities resulted in exceedingly long simulations. Results were then extrapolated with a simple 1D calculation to viscosities up to 10^{12} kPa.s. Results of the 2D simulations show that ascent velocity is inversely proportional to mud viscosity, while the time needed for mud ascent initiation and for mud extrusion is proportional to viscosity (Table 3). When mud overpressure is considered in the simulations, it decreases the time for initiation and extrusion by a ratio of 0.5-0.65 (Table 3). The presence of conduits mainly influences the final width of the gassy-mud column, which decreases with an increasing conduit length (Table 3). Through one-dimensional extrapolation it would take a minimum of 500 years for a buoyant high-viscosity mud to reach the surface if mud overpressure is not considered, while it would take only 100 years if the mud overpressure is integrated in the calculation (Figure 11b). Considering the radius of a conduit (Figure 12b), it arises that the timing for extrusion is significantly increased as it would take more than 10,000 years for the same overpressured mud to reach the surface. Combining 1D and 2D simulations, adapting the Navier-Stokes equations to consider the impact of gas expansion on sediment mass-density through Boyle's law and the influence of mud overpressure over the ascension velocity allowed estimating the time needed for mud generated at depth to reach the seafloor and to form a mud volcano through density-inversion.

781 In the following, the results of the calculations carried out in this paper will be discussed
782 and confronted to previous research to assess the two main questions of the introduction:

- 783 • Is it possible to simulate mud generation conditions at depth by considering the
784 mechanical properties of sediments, the sedimentation rates, structural elements
785 and the impact of gas exsolution?
- 786 • Is the sole impact of gas expansion on the mud properties able to drive mud up to
787 the seafloor?

788 **4.2. Overpressure, hydrofracturing and gas exsolution: from stratified sediments to** 789 **fluid mud**

790 Calculations of pressure related to the maximum gas column that could have been trapped
791 within the ASF (chapter 3, Blouin, 2019) showed that the sole presence of a gas reservoir at the
792 crest of the Absheron fold cannot explain the formation of the Absheron mud volcano, as the
793 fracture pressure was not reached. Hydrofracturing is believed to be necessary to initiate a MV
794 formation as demonstrated through the monitoring of the Lusi initiation (Tingay et al., 2017) and
795 through the analysis of the Absheron Mud Volcano dataset (Blouin et al., 2019a). Therefore,
796 additional parameters are required to explain the AMV formation. The sedimentation rates
797 recorded in the SCB are among the highest in foreland basins (Tagiyev et al., 1997; Allen et
798 al., 2002; Smith-Rouch, 2006; Egan et al., 2009; Green et al., 2009). High sedimentation
799 generates overpressure in low-permeability strata (Dugan & Flemings, 2000; Opara, 2011;
800 Osborne & Swarbrick, 1997) and overpressure is one of the key triggers and drivers for MV
801 formation (Deville, 2009; Dimitrov, 2002; Kopf, 2002; Mazzini & Etiope, 2017).

802 The 2-D diffusion model presented in this paper is based on regional data extracted from
803 literature (Diaconescu et al., 2001; Green et al., 2009), on observations and in situ measurements
804 made on the Absheron gas condensate field, as well as on the laboratory experiments conducted
805 by (Blouin et al., 2019b). The regional-scale pressure gradient and northward fluid circulation
806 from the deep SCB was already observed and discussed by several studies (Bredehoeft et al.,
807 1988; Gautherot et al., 2015; Grosjean et al., 2009; Javanshir et al., 2015), and this type of
808 modeling, studying the influence of regional physical parameters such as sedimentation rate and
809 pressure gradient on local structures such as landslides or venting sites, has already been applied
810 to other sedimentary basins (Dugan & Flemings, 2000; Schneider et al., 2004; Kvalstad et al.,
811 2005; Hustoft et al., 2009). Deville et al. (2010) applied a similar fluid flow numerical model to
812 show that MVs in Trinidad are located above overpressured areas. However, it is the first time,
813 in our knowledge, that a 2D-diffusion model is applied to simulate sediment remobilization into
814 mud at depth.

815 More precise measurements and estimations of layer permeability and fracture pressure
816 would now be needed to improve this simulation. Laboratory testing on rock fragments from the
817 different modeled layers would be necessary to improve their hydro-mechanical properties. Rock
818 cores were sampled at well sites, but only from targeted reservoirs. Therefore, the shallower
819 simulated intervals would already need approximations such as those from this study. Fracturing
820 pressure was only estimated from pressure logs (Blouin et al., 2019a). However, LOT/FIT data
821 indicate that hydrofracturing may occur for an overpressure of 25 MPa. Therefore, less than 2
822 My of overpressure diffusion may be necessary in our simulation in order to obtain the needed
823 25 MPa to trigger fracture generation as the fracture in Figure 6 generated for over 35 MPa of
824 overpressure.

825 The simulation generated a horizontal fractured area where gas exsolved, locally reaching
826 S_g greater than 0.38 and therefore damaging sediments that entirely lost their preconsolidation
827 pressure. This area represents the mud generation zone and is 1300 m long and locally 220 m
828 thick (Figure 6). The presence of the low-permeability ASF prevented pore pressure and
829 therefore fractures to propagate vertically even if the maximum principal stress is vertical, the
830 simulation ignoring the impact of compressive tectonics that are observed over the basin.

831 The 2D modeling presented in this study allows drawing a coupled process for mud
832 generation below the AMV. Due to high sedimentation rates, overpressure is generated in the
833 deeper part of the SCB and is transmitted northwards along under-compacted layers that kept an
834 abnormally high permeability. The fault system at the core of the Absheron anticline leads to
835 local overpressure build-up above the crest of the anticline, eventually initiating hydrofracturing
836 and saturating the pore waters of the Upper Productive Series with methane. Hydrofracturing
837 may trigger a local decrease in overpressure, allowing exsolution of the dissolved methane and
838 triggering sediment damage when S_g exceeds 0.38 (Blouin et al., 2019b). Thus, the 2D diffusion
839 model integrating the mechanical properties of sediments, sedimentation rates,
840 compartmentalization effect of faults and regional seal and the impact of gas exsolution
841 reproduces mud generation conditions at depth below the AMV.

842 **4.3. Mud extrusion resulting from density-inversion driven by gas exsolution**

843 Once mud is generated at depth, it is necessary to understand how it is transferred to the
844 surface. Modeling shows that mud ascent time is proportional to mud viscosity. Taking mud
845 overpressure into account improves the convergence of 1D and 2D results (Figure 11). Similar
846 values of velocity were obtained by Collignon et al. (2018b) who calculated flow rates
847 depending on pipe radius, particle size and density and the type of gas for equivalent viscosities.
848 One-dimensional extrapolation allows to test viscosities closer to those of sedimentary rocks,
849 which was not possible on the 2D simulations due to time limitations. It would take
850 approximately 100 years for the mud generated at the AMV location to rise to the surface if mud
851 was only transported through density inversion and mud overpressure. The link between 2D
852 results and the extrapolation in 1D may not straightforward. The extrapolation in 1D is made
853 over 6 orders of magnitude of viscosities and compared to only two 2D control points. The
854 relationship between mud remobilization and the host sediment viscosity may not be a linear
855 process when dealing with high values of μ . Therefore, the results have to be addressed with
856 caution. Nevertheless, some MVs display very slow extrusion rates, such as the Kotyrdag
857 (onshore Azerbaijan), that extrudes high viscosity and slightly wet mud with an estimated rate of
858 0.02 m/day (Dupuis, 2017), in other words 2.3×10^{-7} m/s, which is the order of magnitude
859 obtained from our modeling.

860 The presence of a preexisting conduit in our simulations modifies the extrusion time, but
861 it reduces the extrusion rate as a smaller volume of mud is able to rise through the sedimentary
862 column. One-dimensional calculations considering fracture radius show that the extrusion time is
863 close to 10,000 years for $\mu = 10^{12}$ kPa.s. The simulations shown here do not address multi-phase
864 flow, gas being only considered in the mass-density calculation. If free-gas was able to flow
865 directly through the fracture, it may be able to fracture and/or damage shallower sediments,
866 forming a secondary mud generation zone. This was observed at Lusi, where the BJP-1 well
867 transferred overpressured fluids charged with gas to shallower and more fragile strata, triggering
868 hydrofractures and mud generation (Tingay et al., 2008; Tingay et al., 2015).

869 In contrast to our numerical model in which mud ascent occurs along a unique wide
870 fracture, field work reported by Roberts et al. (2010) seems to indicate that mud volcano
871 conduits rather consist of an intricate and complex fractured volume with detached and rotated
872 blocks. Roberts et al. (2010) explain their observations by the rising of overpressured and low-
873 density mud that generates and propagates fractures as it rises, slowly opening its way up to the
874 surface. Thus, the 2D simulations should rather compute the progressive opening of fractures as
875 mud overpressure increases due to gas expansion. This would imply a combination of solid-rock
876 mechanics and fluid mechanics that represents a complete field of research in modeling and
877 computation, notably applied to hydrofracturing issues in well bores (Mainguy & Longuemare,
878 2002; Wu & Olson, 2015). The Lusi catastrophe allowed to monitor the initiation of a mud
879 volcano formation. From the analysis of drilling reports, and notably records on the expelled gas,
880 drilling mud losses and drilling mud pressure, Tingay et al. (2017) show that 24-48 hours
881 separate the moment when free-gas was detected at the bottom of the well, and the moment when
882 the mud extruded at the surface. Therefore, gas-driven mud generation and transport seem to
883 occur very fast. Our model points to a transport duration of 100 years to cross the 3000 meters of
884 strata separating the mud source from the surface but through the sole density inversion driven
885 by gas expansion. The impact of gas expansion on overpressure and on rock failure is not
886 explored but is expected to reduce significantly the time for extrusion. Besides, this combination
887 of processes would imply a similar plumbing system as the one described by Roberts et
888 al. (2010).

889 Another limitation of the current model is that the influence of gas exsolution on mud
890 rheology was not accounted for. The presence of gas and liquids in the mud are known to
891 strongly affect its viscosity (Kopf, 2002; Mazzini & Etiope, 2017). Collignon et al. (2018b) and
892 Zoporowski & Miller (2009) both have considered a dynamic viscosity in their simulations and
893 shows that the contrast between mud viscosity and the viscosity of the surrounding rock
894 increases flow rates. Modeling results of Collignon et al. (2018b) demonstrated that the feeding
895 pipe of the Lusi MV has to be smaller than 1.5 m radius in order to match its maximal mud
896 discharge, when our model displays very long extrusion time for small fractures. Thus, the
897 integration of a dynamic viscosity depending on gas content would certainly increase the
898 velocity of the extrusion process in our model. It will also allow to study the effect of low-
899 viscosity layers, for instance containing evaporites like the ASF. Besides, the gas mass-density
900 was considered negligible in the calculation of the mud mass-density. However, gas mass-
901 density depends on the pressure and temperature conditions, and represents 1/5 of the water
902 mass-density at 35 MPa and 50 °C.

903 Finally, the code of Tryggvason (2012) was developed to answer fluid mechanics issues.
904 Working with values corresponding to a geological background leads to very long calculation
905 time due to computing limitations arising from the resolution method. Therefore, the code should
906 be improved or another resolution method should be explored in order to run 2D simulations
907 with parameters fitting the geological reality over shorter periods of time.

908 The sole effect of gas expansion on the mud mass-density is thus able to drive mud ascent
909 up to the seafloor. The process may be accelerated if the influence of gas exsolution and
910 expansion on mud viscosity and of fracture propagation ahead of the rising mud are accounted
911 for. This modeling work resulted in extrusion rates of the same order of magnitude that what has
912 been observed on MVs extruding high viscosity mud.

913 **4.4. Towards a quantitative formation model for the Absheron mud volcano**

914 The conceptual formation model for the AMV presented in Blouin et al. (2019a) was
915 improved by integrating the main findings of Blouin et al. (2019b) and of the numerical models.
916 This allows to move from a purely qualitative model, to a semi-quantitative one including the
917 formation dynamics as a function of the main physical parameters controlling the mud volcano
918 formation: ratio of overpressure to vertical effective stress, dissolved methane concentration and
919 degree of gas saturation. The updated formation model is composed of 7 different phases shown
920 in the different panels of Figure 13:

921 Phase 1 - At 3.4 Ma, end of the rapid deposition of the Productive Series (over 3.5 km in
922 2 My) above the gas-mature Maykop Formation that generated hydrocarbons diffusing slowly
923 through the sedimentary column (Figure 13a). The Maykop Formation started generating gas
924 during the Late Miocene in the Shah Deniz region located in a structural setting comparable to
925 Absheron (figure 2.9 in Alizadeh et al., 2017). Moreover, the deposition of the Anhydritic
926 Surakhany Formation provided an efficient seal allowing a slow and uniform overpressure build-
927 up in the Productive Series generated by high sedimentation rates.

928 Phase 2 – At 0.7 Ma, the growth rate of the Absheron fold increased significantly.
929 Methane circulation was therefore focused into the faulted core of the anticline (Figure 13b). The
930 difference of overburden between the anticline and adjacent syncline generated an overpressure
931 gradient leading to overpressure build-up against the sealing faults (Figure 13b). Besides, at the
932 anticline crest, the vertical effective stress σ'_v is lower than on the flanks due to reduced
933 overburden thickness. Thus, overpressure generation and transmission as well as low σ'_v at the
934 crest increased the $\Delta u / \sigma'_v$ ratio.

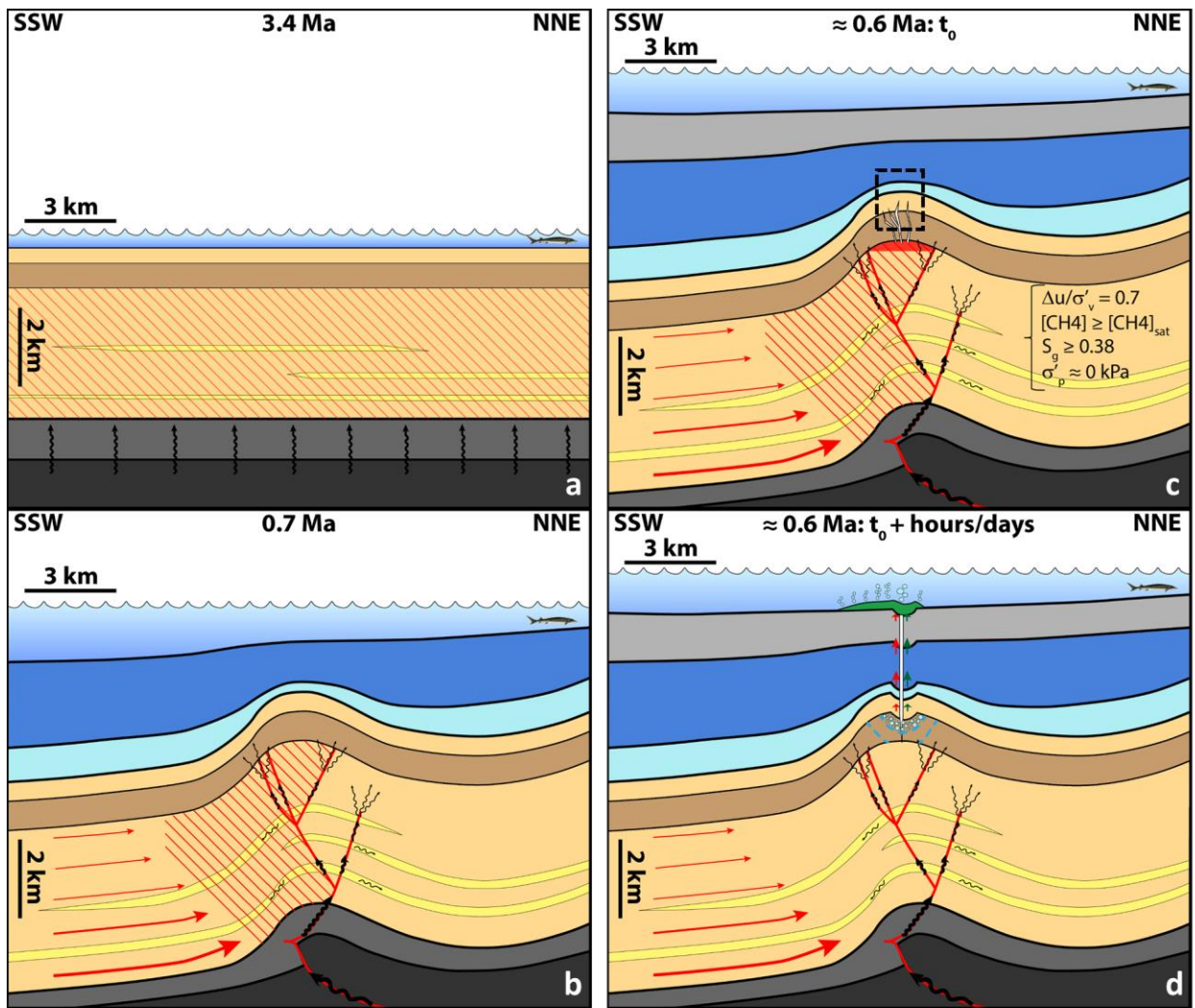
935 Phase 3 – At ≈ 0.6 Ma, $\Delta u / \sigma'_v$ reached the hydro-fracturing threshold of 0.7 (Figure 13c),
936 allowing hydrofracturing. This led to a local decrease of overpressure through fluid dissipation
937 and triggered methane exsolution where the dissolved-methane concentration reached the
938 methane solubility (Henry's law; Figure 13c). For a gas saturation higher than 0.38, the sediment
939 lost its preconsolidation pressure leading to mud generation (Figure 13c).

940 Phase 4 – The presence of gas bubbles in the mud significantly reduced its mass-density
941 and its viscosity (Figure 13g). Therefore, the gassy mud started to rise along the open fractures.
942 As gas bubbles moved up, they expanded (following Boyles's law), hence increasing gas
943 saturation and decreasing the mud mass-density and viscosity (Figure 13g). Thus, mud velocity
944 increased as bubbles expanded. Gas expansion maintained the overpressure as mud rose along
945 fractures, leading to a critical value of $\Delta u / \sigma'_v$ and to fracture propagation towards the surface
946 (Figure 13g). This stage should have happened over a short period of time, ranging from hours to
947 days.

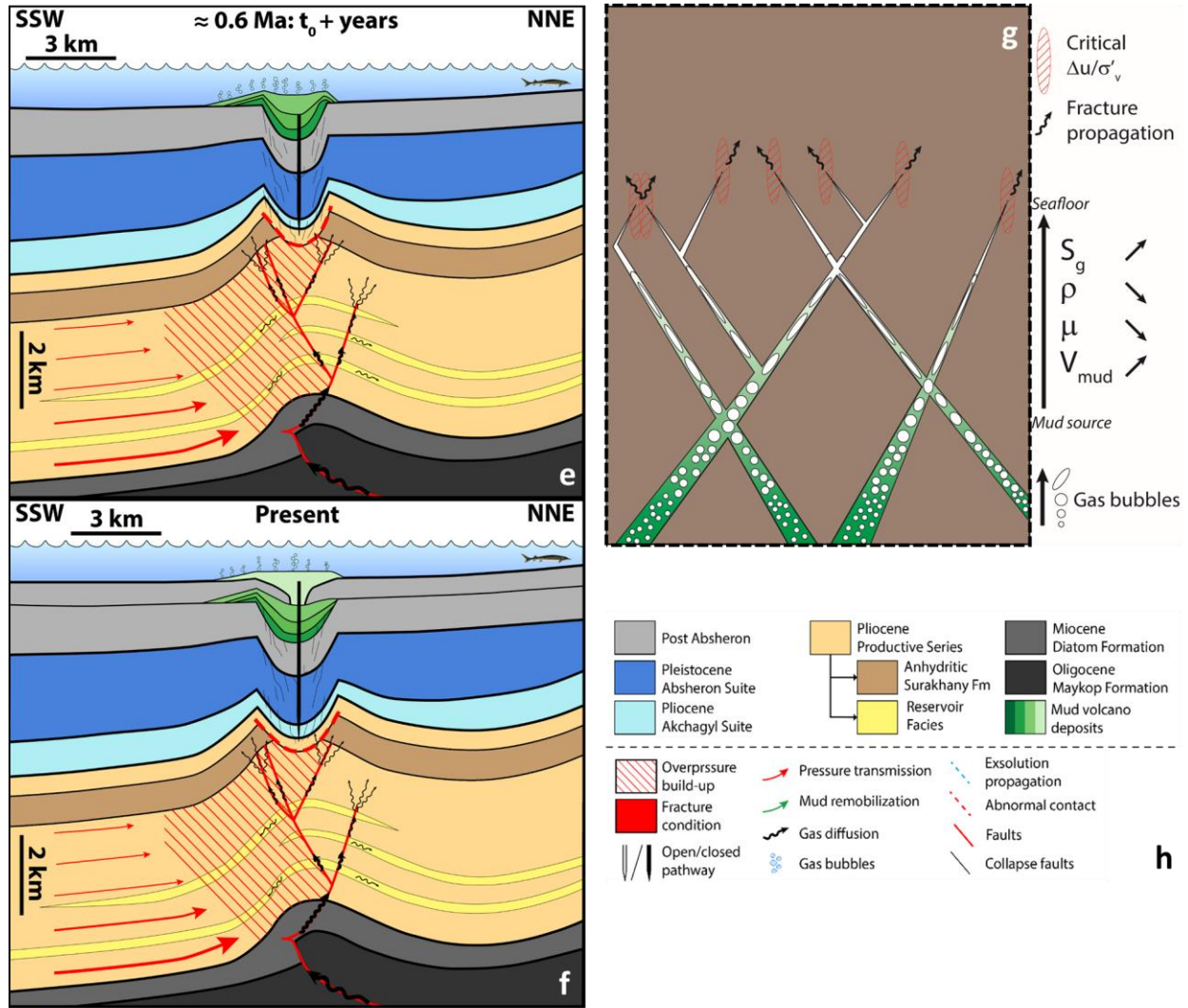
948 Phase 5 – After several days, the fractured “pipe” connected the mud generation zone,
949 where gas exsolution was still damaging sediments, with the seafloor (Figure 13d). First mud
950 extrusion happened at the seafloor leading to the progressive formation of the extrusive edifice,
951 while mud slowly degassed in the water column (Figure 13d). This direct hydraulic connection
952 prevented overpressure from building up again at depth as it was directly transmitted to the
953 surface (Figure 13d), thus preventing gas exsolution from stopping. At depth, the extrusion of
954 remobilized mud slowly led to roof collapse, progressively forming what is known as a
955 “depletion zone” (Dupuis et al., 2019; Kirkham et al., 2017; Stewart & Davies, 2006).

956 Phase 6 – After several years, multiple mud extrusion episodes reached the surface as the
 957 depletion zone became bigger along with the collapse of the overlying strata, forming a giant
 958 mud shield at the seafloor (Figure 13e). The AMV then entered a quiescent phase. Overpressure
 959 was not maintained high enough to keep fractures open and overpressure built up again along the
 960 sealing faults, preventing further gas exsolution (Figure 13e).

961 Phase 7 – Present day geometry, after multiple phases of quiescence and activity, creating
 962 a complex interdigitated geometry where normal sedimentation predominates during quiescent
 963 phases of the volcano. When $\Delta u / \sigma'_v$ reaches the fracture opening threshold, further depletion
 964 happens in the source, enhancing collapse, while more mud is extruded at the seafloor during the
 965 active phases (Figure 13f).



966
 967



968

969

970

971

972

Figure 13: Formation model for the Absheron mud volcano based on in situ observations and measurements, sediment analysis, laboratory testing and mud generation and remobilization numerical modeling. Details of the different stages displayed in a, b, c, d, e, and f and g are in the text. g is a zoom corresponding to black dotted rectangle in c, and shows the processes involved in of mud remobilization towards the surface. h: legend corresponding to a, b, c, d, e and f.

973

5. Conclusion

974

975

976

977

978

979

980

981

This study explored the possibility of simulating mud generation and extrusion processes through numerical modeling based on simplified physical principles. The ultimate goal is to simulate the complete formation of the Absheron Mud Volcano (AMV) and to quantify the overpressure conditions and methane concentration that led to the present structure. A first model, considering 2D-diffusion laws (Darcy's law and Fick's law) was used to explain the location of the AMV as well as the conditions required to generate fluid mud from stratified solid sediments. The second model applies a fluid mechanics approach to test whether the sole impact of gas expansion on the mud density can lead to mud extrusion. The main results are:

982

983

984

- 1- The 2D-diffusion model showed that using sedimentation rates corrected from compaction to calculate overpressure in the deep basin and considering the low-permeability Anhydritic Surakhany Formation and sealing faults as flow baffles,

- 985 critical fracture conditions are obtained at the crest of the Absheron anticline, below
986 the ASF, where the depleted area was observed by Blouin et al. (2019).
987 2- A methane concentration of 5550 mM, imposed at the base of the fault network
988 considered as permeable in the vertical direction creates the conditions for triggering
989 gas exsolution and subsequent loss in preconsolidation pressure showing that liquid
990 mud is generated at depth.
991 3- Mud ascent up to the seafloor through the sole density-inversion provoked by gas
992 expansion is possible over a period of 100 years minimum. This period of time for
993 extrusion corresponds to extrusion rates measured at particular MVs.
994 4- To accelerate the process, additional parameters such as non-constant viscosity and
995 the upward propagation of fracture as consequences of gas expansion have to be
996 considered.
997 5- The results allow going from a purely conceptual formation model to a semi-
998 quantitative model considering dynamics of the processes involved and quantification
999 of the main controlling physical parameters.

1000 We show that simple physical models integrating realistic geological and hydro-
1001 mechanical parameters and behavior of sediments are able to reproduce the conditions that
1002 initiated the formation of the Absheron Mud Volcano. We simulated the key processes inferred
1003 from the available dense dataset and from the present geometry that were described in the
1004 conceptual model in Blouin et al. (2019). A dense and high-quality dataset is paramount to
1005 complete such models using the same methodology on other mud volcanoes located in similar
1006 contexts.

1007 **Acknowledgments, Samples, and Data**

1008 This study was realized in the scope of the PhD of Arthur Blouin under the joint direction
1009 of the Pau University (UPPA), Ifremer and Total S.A. To access the SeCoV3 software and
1010 output of the different presented simulations and calculations, please directly download it here
1011 <https://doi.org/10.6084/m9.figshare.12052965.v2>.

1012 **References**

- 1013 Abreu, V., & Nummedal, D. (2007). Miocene to Quaternary Sequence Stratigraphy of the South
1014 and Central Caspian Basins. *AAPG Studies in Geology*, 55, 65–86.
1015 <https://doi.org/10.1306/1205845St553000>
- 1016 Alizadeh, A. A., Guliyev, I. S., Kadirov, F. A., & Eppelbaum, L. V. (2017). *Geosciences of*
1017 *Azerbaijan Volume II: Economic Geology and Applied Geophysics* (Vol. II). Basel:
1018 Springer International Publishing Switzerland. <https://doi.org/10.1007/978-3-319-40493-6>
- 1019 Allen, M. B., Jones, S., Ismail-Zadeh, A., Simmons, M., & Anderson, L. (2002). Onset of
1020 subduction as the cause of rapid Pliocene-Quaternary subsidence in the South Caspian
1021 basin. *Geology*, 30(9), 775–778. [https://doi.org/10.1130/0091-](https://doi.org/10.1130/0091-7613(2002)030<0775:OOSATC>2.0.CO;2)
1022 [7613\(2002\)030<0775:OOSATC>2.0.CO;2](https://doi.org/10.1130/0091-7613(2002)030<0775:OOSATC>2.0.CO;2)
- 1023 Battani, A., Prinzhofer, A., Deville, E., & Ballentine, C. J. (2010). Trinidad Mud Volcanoes: The
1024 Origin of the Gas. *Shale Tectonics: AAPG Memoir*, 93, 225–238.

- 1025 <https://doi.org/10.1306/13231317M933427>
- 1026 Blouin, A. (2019). *Formation de boue à partir de sédiments stratifiés dans un contexte de*
1027 *volcanisme de boue: le rôle du gaz*. Université de Pau et des Pays de l'Adour.
- 1028 Blouin, A., Imbert, P., Sultan, N., & Callot, J. (2019). Evolution model for the Absheron mud
1029 volcano: from in - situ observations to numerical modeling. *Journal of Geophysical*
1030 *Research: Earth Surface*, 124(3), 766–794. <https://doi.org/10.1029/2018JF004872>
- 1031 Blouin, A., Sultan, N., Callot, J., & Imbert, P. (2019). Sediment damage caused by gas
1032 exsolution: a key mechanism for mud volcano formation. *Engineering Geology*, 263.
- 1033 Bredehoeft, J. D., Djevanshir, R. D., & Belitz, K. R. (1988). Lateral fluid flow in a compacting
1034 sand-shale sequence: South Caspian basin. *American Association of Petroleum Geologists*
1035 *Bulletin*, 72(4), 416–424. [https://doi.org/10.1306/703C9A1E-1707-11D7-](https://doi.org/10.1306/703C9A1E-1707-11D7-8645000102C1865D)
1036 [8645000102C1865D](https://doi.org/10.1306/703C9A1E-1707-11D7-8645000102C1865D)
- 1037 Brown, K. M. (1990). The nature and hydrogeologic significance of mud diapirs and diatremes
1038 for accretionary systems. *Journal of Geophysical Research*, 95(B6), 8969.
1039 <https://doi.org/10.1029/JB095iB06p08969>
- 1040 Caine, J. S., Evans, J. P., & Forster, C. B. (1996). Fault zone architecture and permeability
1041 structure. *Geology*, 24(11), 1025–1028. [https://doi.org/https://doi.org/10.1130/0091-](https://doi.org/https://doi.org/10.1130/0091-7613(1996)024<1025:FZAAPS>2.3.CO;2)
1042 [7613\(1996\)024<1025:FZAAPS>2.3.CO;2](https://doi.org/https://doi.org/10.1130/0091-7613(1996)024<1025:FZAAPS>2.3.CO;2)
- 1043 Collignon, M., Mazzini, A., Schmid, D. W., & Lupi, M. (2018). Modelling fluid flow in active
1044 clastic piercements: Challenges and approaches. *Marine and Petroleum Geology*, 90, 157–
1045 172. <https://doi.org/10.1016/j.marpetgeo.2017.09.033>
- 1046 Collignon, M., Schmid, D. W., Galerne, C., Lupi, M., & Mazzini, A. (2018). Modelling fluid
1047 flow in clastic eruptions: Application to the Lusi mud eruption. *Marine and Petroleum*
1048 *Geology*, 90, 173–190. <https://doi.org/10.1016/j.marpetgeo.2017.08.011>
- 1049 Contet, J., & Unterseh, S. (2015). Multiscale site investigation of a giant mud-volcano offshore
1050 Azerbaijan - Impact on subsea field development. *Offshore Technology Conference, OTC-*
1051 *25864(Mv)*, 1–10. <https://doi.org/10.4043/25864-MS>
- 1052 DeGroot, D. J., Lunne, T., & Tjelta, T. I. (2010). Recommended best practise for geotechnical
1053 site characterisation of cohesive offshore sediments. In S. Gourvenec & D. White (Eds.),
1054 *Frontiers in Offshore Geotechnics II* (pp. 33–57). Perth, Australia: CRC Press, Taylor &
1055 Francis Group.
- 1056 Deville, E. (2009). Mud Volcano Systems. In N. Lewis & A. Moretti (Eds.), *Volcanoes:*
1057 *Formation, Eruptions and Modelling* (pp. 95-125 (404)). Nova Science Publishers.
- 1058 Deville, Eric, Guerlais, S. H., Lallemand, S., & Schneider, F. (2010). Fluid dynamics and
1059 subsurface sediment mobilization processes: An overview from Southeast Caribbean. *Basin*
1060 *Research*, 22(4), 361–379. <https://doi.org/10.1111/j.1365-2117.2010.00474.x>

- 1061 Diaconescu, C. C., Kieckhefer, R. M., & Knapp, J. H. (2001). Geophysical evidence for gas
1062 hydrates in the deep water of the South Caspian Basin, Azerbaijan. *Marine and Petroleum*
1063 *Geology*, 18(2), 209–221. [https://doi.org/10.1016/S0264-8172\(00\)00061-1](https://doi.org/10.1016/S0264-8172(00)00061-1)
- 1064 Dimitrov, L. I. (2002). Mud volcanoes-the most important pathway for degassing deeply buried
1065 sediments. *Earth-Science Reviews*, 59(1–4), 49–76. [https://doi.org/10.1016/S0012-](https://doi.org/10.1016/S0012-8252(02)00069-7)
1066 [8252\(02\)00069-7](https://doi.org/10.1016/S0012-8252(02)00069-7)
- 1067 Duan, Z., & Mao, S. (2006). A thermodynamic model for calculating methane solubility, density
1068 and gas phase composition of methane-bearing aqueous fluids from 273 to 523 K and from
1069 1 to 2000 bar. *Geochimica et Cosmochimica Acta*, 70(13), 3369–3386.
1070 <https://doi.org/10.1016/j.gca.2006.03.018>
- 1071 Dugan, B., & Flemings, P. (2000). Overpressure and fluid flow in the new jersey continental
1072 slope: implications for slope failure and cold seeps. *Science (New York, N.Y.)*, 289(July),
1073 288–291. <https://doi.org/10.1126/science.289.5477.288>
- 1074 Dupuis, M. (2017). *Processus de mise en place et évolution des systèmes de volcans de boue.*
1075 Université Lille 1 - Sciences et technologies.
- 1076 Dupuis, M., Imbert, P., Odonne, F., & Vendeville, B. (2019). Mud volcanism by repeated roof
1077 collapse : 3D architecture and evolution of a mud volcano cluster off shore Nigeria. *Marine*
1078 *and Petroleum Geology*, 110(July), 368–387.
1079 <https://doi.org/10.1016/j.marpetgeo.2019.07.033>
- 1080 Egan, S. S., Mosar, J., Brunet, M.-F., & Kangarli, T. (2009). Subsidence and uplift mechanisms
1081 within the South Caspian Basin: insights from the onshore and offshore Azerbaijan region.
1082 *Geological Society, London, Special Publications*, 312(1), 219–240.
1083 <https://doi.org/10.1144/SP312.11>
- 1084 Esrig, M. I., & Kirby, R. C. (1977). Implications of gas content for predicting the stability of
1085 submarine slopes. *Marine Geotechnology*, 2(1–4), 81–100.
1086 <https://doi.org/10.1080/10641197709379771>
- 1087 Etiope, G., Feyzullayev, A., & Baci, C. L. (2009). Terrestrial methane seeps and mud
1088 volcanoes: A global perspective of gas origin. *Marine and Petroleum Geology*, 26(3), 333–
1089 344. <https://doi.org/10.1016/j.marpetgeo.2008.03.001>
- 1090 Evans, J. P., Forster, C. B., & Goddard, J. V. (1997). Permeability of fault-related rocks , and
1091 implications for hydraulic structure of fault zones. *Journal of Structural Geology*, 19(11),
1092 1393–1404. [https://doi.org/https://doi.org/10.1016/S0191-8141\(97\)00057-6](https://doi.org/https://doi.org/10.1016/S0191-8141(97)00057-6)
- 1093 Forte, A. M., & Cowgill, E. (2013). Late Cenozoic base-level variations of the Caspian Sea: A
1094 review of its history and proposed driving mechanisms. *Palaeogeography,*
1095 *Palaeoclimatology,* *Palaeoecology*, 386, 392–407.
1096 <https://doi.org/10.1016/j.palaeo.2013.05.035>
- 1097 Furbish, D. J. (1997). *Fluid Physics in Geology*. New York: Oxford University Press.

- 1098 Gautherot, T., Total, S. A., Bakirov, S., Upstream, S., & International, M. (2015). Absheron
1099 Field – ABX-2 Exploration Drilling Challenges and Realizations Return to Absheron field,
1100 (June 2009), 4–6.
- 1101 Gisler, G. (2009). Simulations of the explosive eruption of superheated fluids through
1102 deformable media. *Marine and Petroleum Geology*, 26(9), 1888–1895.
1103 <https://doi.org/10.1016/j.marpetgeo.2008.12.006>
- 1104 Gordon, D. S., & Flemings, P. B. (1998). Generation of overpressure and compaction-driven
1105 fluid flow in a Plio-Pleistocene Eugene Island 330 , offshore Louisiana. *Basin Research*, 10,
1106 177–196.
- 1107 Grauls, D. J., & Baleix, J. M. (1994). Role of overpressures and in situ stresses in fault-
1108 controlled hydrocarbon migration : a case study. *Marine and Petroleum Geology*, 11(6),
1109 734–742.
- 1110 Green, T., Abdullayev, N., Hossack, J., Riley, G., & Roberts, A. M. (2009). Sedimentation and
1111 subsidence in the South Caspian Basin, Azerbaijan. *Geological Society, London, Special
1112 Publications*, 312(1), 241–260. <https://doi.org/10.1144/SP312.12>
- 1113 Grosjean, Y., Zaugg, P., Gaulier, J.-M., & Total S.A. (2009). Burial Hydrodynamics and Subtle
1114 Hydrocarbon Trap Evaluation : From the Mahakam Delta to the South Caspian Sea.
1115 *International Petroleum Technology Conference Held in Doha, Qatar, 7-9 December 2009*,
1116 1–12.
- 1117 Guliyev, I., Aliyeva, E., Huseynov, D., Feyzullayev, A., & Mamedov, P. (2011). Hydrocarbon
1118 Potential of Ultra Deep Deposits in the South Caspian Basin. In *AAPG European Region
1119 Annual Conference* (Vol. 1, p. 66). Kiev, Ukraine.
- 1120 Henry, P., Guglielmi, Y., Gout, C., Castilla, R., Dick, P., Donzé, F., et al. (2019). Strain and flow
1121 pathways in a shale fault zone : An in-situ test of fault seal integrity. In *Fifth International
1122 Conference on Fault and Top Seals* (pp. 8–12). Palermo, Italy: EAGE Publications.
- 1123 Hight, D. W., Hamza, M. M., & El Sayed, A. S. (2002). Engineering characterization of the Nile
1124 Delta clays. In A. Nakase & T. Tsuchida (Eds.), *Coastal geotechnical engineering in
1125 practice* (pp. 149–162). Lisse, the Netherlands: Swets & Zeitlinger.
- 1126 Hinds, D. J., Aliyeva, E., Allen, M. B., Davies, C. E., Kroonenberg, S. B., Simmons, M. D., &
1127 Vincent, S. J. (2004). Sedimentation in a discharge dominated fluvial-lacustrine system:
1128 The Neogene Productive Series of the South Caspian Basin, Azerbaijan. *Marine and
1129 Petroleum Geology*, 21(5), 613–638. <https://doi.org/10.1016/j.marpetgeo.2004.01.009>
- 1130 Hubbert, M. K. (1937). Theory of scale models as applied to the study of geologic structures.
1131 *Bulletin of the Geological Society of America*, 48, 1459–1520.
- 1132 Hustoft, S., Dugan, B., & Mienert, J. (2009). Effects of rapid sedimentation on developing the
1133 Nyegga pockmark field: Constraints from hydrological modeling and 3-D seismic data,
1134 offshore mid-Norway. *Geochemistry, Geophysics, Geosystems*, 10(6).

- 1135 <https://doi.org/10.1029/2009GC002409>
- 1136 Imbert, P., Geiss, B., & Fatjó de Martín, N. (2014). How to evacuate 10 km³ of mud: Saturate
1137 with gas and decrease the pressure! *Geo-Marine Letters*, 34(2–3), 199–213.
1138 <https://doi.org/10.1007/s00367-014-0357-3>
- 1139 Inan, S., Namik Yalçın, M., Guliev, I. S., Kuliev, K., & Akper Feizullayev, A. (2002). Deep
1140 petroleum occurrences in the Lower Kura Depression, South Caspian Basin, Azerbaijan: an
1141 organic geochemical and basin modeling study. *Marine and Petroleum Geology*, 14(7–8),
1142 731–762. [https://doi.org/10.1016/s0264-8172\(97\)00058-5](https://doi.org/10.1016/s0264-8172(97)00058-5)
- 1143 Javanshir, R. J., Riley, G. W., Duppenbecker, S. J., & Abdullayev, N. (2015). Validation of
1144 lateral fluid flow in an overpressured sand-shale sequence during development of Azeri-
1145 Chirag-Gunashli oil field and Shah Deniz gas field: South Caspian Basin, Azerbaijan.
1146 *Marine and Petroleum Geology*, 59, 593–610.
1147 <https://doi.org/10.1016/j.marpetgeo.2014.07.019>
- 1148 Jeong, S. W. (2013). Determining the viscosity and yield surface of marine sediments using
1149 modified Bingham models. *Geosciences Journal*, 17(3), 241–247.
1150 <https://doi.org/10.1007/s12303-013-0038-7>
- 1151 Kirkham, C., Cartwright, J., Hermanrud, C., & Jebsen, C. (2017). The genesis of mud volcano
1152 conduits through thick evaporite sequences. *Basin Research*, 1–20.
1153 <https://doi.org/10.1111/bre.12250>
- 1154 Kopf, A. J. (2002). Significance of mud volcanism. *Reviews of Geophysics*, 40(2), 1005.
1155 <https://doi.org/10.1029/2000RG000093>
- 1156 Kvalstad, T. J., Andresen, L., Forsberg, C. F., Berg, K., Bryn, P., & Wangen, M. (2005). The
1157 Storegga slide: Evaluation of triggering sources and slide mechanics. *Marine and Petroleum*
1158 *Geology*, 22(1-2 SPEC. ISS.), 245–256. <https://doi.org/10.1016/j.marpetgeo.2004.10.019>
- 1159 Lafuerza, S., Sultan, N., Canals, M., Lastras, G., Cattaneo, A., Frigola, J., et al. (2012). Failure
1160 mechanisms of Ana Slide from geotechnical evidence, Eivissa Channel, Western
1161 Mediterranean Sea. *Marine Geology*, 307–310, 1–21.
1162 <https://doi.org/10.1016/j.margeo.2012.02.010>
- 1163 Lawrence, G. W. M., & Cartwright, J. A. (2010). The stratigraphic and geographic distribution
1164 of giant craters and remobilised sediment mounds on the mid Norway margin, and their
1165 relation to long term fluid flow Slide W. *Marine and Petroleum Geology*, 27(4), 733–747.
1166 <https://doi.org/10.1016/j.marpetgeo.2009.10.012>
- 1167 Locat, J., & Demers, D. (2008). Viscosity, yield stress, remolded strength, and liquidity index
1168 relationships for sensitive clays. *Canadian Geotechnical Journal*, 25(4), 799–806.
1169 <https://doi.org/10.1139/t88-088>
- 1170 Lunne, T., Berre, T., Strandvik, S., Andersen, K. H., & Tjelta, T. I. (2001). Deepwater sample
1171 disturbance due to stress relief. In *Proceedings of the 1st Annual Offshore Technology*

- 1172 *Conference* (pp. 64–85). Houston, Texas.
- 1173 Mainguy, M., & Longuemare, P. (2002). Coupling Fluid Flow and Rock Mechanics :
1174 Formulations of the Partial Coupling between Reservoir and Geomechanical Simulators. *Oil*
1175 & *Gas Science and Technology*, 57(4), 355–367.
- 1176 Mazzini, A., & Etiope, G. (2017). Mud volcanism: An updated review. *Earth-Science Reviews*,
1177 168, 81–112. <https://doi.org/10.1016/j.earscirev.2017.03.001>
- 1178 Mazzini, Adriano, Etiope, G., & Svensen, H. (2012). A new hydrothermal scenario for the 2006
1179 Lusi eruption, Indonesia. Insights from gas geochemistry. *Earth and Planetary Science*
1180 *Letters*, 317–318(May 2006), 305–318. <https://doi.org/10.1016/j.epsl.2011.11.016>
- 1181 Morley, C. K., von Hagke, C., Hansberry, R., Collins, A., Kanitpanyacharoen, W., & King, R.
1182 (2017). Review of major shale-dominated detachment and thrust characteristics in the
1183 diagenetic zone: Part I, meso- and macro-scopic scale. *Earth-Science Reviews*, 172(May).
1184 <https://doi.org/10.1016/j.earscirev.2017.07.019>
- 1185 Morton, A., Allen, M., Simmons, M., Spathopoulos, F., Still, J., Hinds, D., et al. (2003).
1186 Provenance patterns in a neotectonic basin: Pliocene and quaternary sediment supply to the
1187 South Caspian. *Basin Research*, 15(3), 321–337. [https://doi.org/10.1046/j.1365-](https://doi.org/10.1046/j.1365-2117.2003.00208.x)
1188 [2117.2003.00208.x](https://doi.org/10.1046/j.1365-2117.2003.00208.x)
- 1189 Mourgues, R., Bureau, D., Bodet, L., Gay, A., & Gressier, J. B. (2012). Formation of conical
1190 fractures in sedimentary basins: Experiments involving pore fluids and implications for
1191 sandstone intrusion mechanisms. *Earth and Planetary Science Letters*, 313–314(1), 67–78.
1192 <https://doi.org/10.1016/j.epsl.2011.10.029>
- 1193 Mukherjee, S., Talbot, C. J., & Koyi, H. A. (2010). Viscosity estimates of salt in the Hormuz and
1194 Namakdan salt diapirs , Persian Gulf. *Geology Magazine*, 147(4), 497–507.
1195 <https://doi.org/10.1017/S001675680999077X>
- 1196 Nermoen, A., Galland, O., Jettestuen, E., Fristad, K., Podladchikov, Y., Svensen, H., & Malthe-
1197 Srenssen, A. (2010). Experimental and analytic modeling of piercement structures. *Journal*
1198 *of Geophysical Research: Solid Earth*, 115(10), 1–15.
1199 <https://doi.org/10.1029/2010JB007583>
- 1200 Odonne, F., Imbert, P., Dupuis, M., Aliyev, A. A., Abbasov, O. R., Baloglanov, E. E., et al.
1201 (2020). Mud volcano growth by radial expansion : Examples from onshore Azerbaijan.
1202 *Marine and Petroleum Geology*, 112(September 2019), 104051.
1203 <https://doi.org/10.1016/j.marpetgeo.2019.104051>
- 1204 Opara, A. I. (2011). ESTIMATION OF MULTIPLE SOURCES OF OVERPRESSURES
1205 USING VERTICAL EFFECTIVE STRESS APPROACH: CASE STUDY OF THE
1206 NIGER DELTA , NIGERIA. *Petroleum & Coal*, 53(4), 302–314.
- 1207 Osborne, M. J., & Swarbrick, R. E. (1997). Mechanisms for Generating Overpressure in
1208 Sedimentary Basins : A Reevaluation 1. *AAPG Bulletin*, 6(6), 1023–1041.

- 1209 PCDM. (2018). Calculateur principal, DATARMOR. Retrieved August 27, 2019, from
1210 <https://wwz.ifremer.fr/pcdm/Equipement>
- 1211 Priest, J. A., Clayton, C. R. I., & Rees, E. V. L. (2014). Potential impact of gas hydrate and its
1212 dissociation on the strength of host sediment in the Krishna-Godavari Basin. *Marine and*
1213 *Petroleum Geology*, 58(PA), 187–198. <https://doi.org/10.1016/j.marpetgeo.2014.05.008>
- 1214 Riboulot, V., Cattaneo, A., Sultan, N., Garziglia, S., Ker, S., Imbert, P., & Voisset, M. (2013).
1215 Sea-level change and free gas occurrence influencing a submarine landslide and pockmark
1216 formation and distribution in deepwater Nigeria. *Earth and Planetary Science Letters*, 375,
1217 78–91. <https://doi.org/10.1016/j.epsl.2013.05.013>
- 1218 Roberts, K. S., Davies, R. J., & Stewart, S. A. (2010). Structure of exhumed mud volcano feeder
1219 complexes, Azerbaijan. *Basin Research*, 22(4), 439–451. <https://doi.org/10.1111/j.1365-2117.2009.00441.x>
- 1221 Schneider, F., Pagel, M., & Hernandez, E. (2004). Basin Modeling in a Complex Area: Example
1222 from the Eastern Venezuelan Foothills. In R. Swennen, F. Roure, & J. W. Granath (Eds.),
1223 *Deformation, fluid flow, and reservoir appraisal in foreland fold and thrust belts* (pp. 357–
1224 369). AAPG Hedberg Series. <https://doi.org/10.1306/1025700H1504>
- 1225 Sibson, R. H. (2003). Brittle-failure controls on maximum sustainable overpressure in different
1226 tectonic regimes. *American Association of Petroleum Geologists Bulletin*, 87(6), 901–908.
1227 <https://doi.org/10.1306/01290300181>
- 1228 Smith-Rouch, L. S. (2006). Oligocene-Miocene Maykop/Diatom Total Petroleum System of the
1229 South Caspian Basin Province, Azerbaijan, Iran, and Turkmenistan. *U.S. Geological Survey*
1230 *Bulletin*, 2201–I, 27.
- 1231 Stewart, S. A., & Davies, R. J. (2006). Structure and emplacement of mud volcano systems in the
1232 South Caspian Basin. *AAPG Bulletin*, 90(5), 771–786. <https://doi.org/10.1306/11220505045>
- 1233 Sultan, N., Savoye, B., Jouet, G., Leynaud, D., Cochonat, P., Henry, P., et al. (2010).
1234 Investigation of a possible submarine landslide at the Var delta front (Nice slope - SE
1235 France). *Canadian Geotechnical Journal*, 47(4), 486–496.
- 1236 Sultan, N., De Gennaro, V., & Puech, A. (2012). Mechanical behaviour of gas-charged marine
1237 plastic sediments. *Géotechnique*, 62(9), 751–766. <https://doi.org/10.1680/geot.12.OG.002>
- 1238 Tagiyev, M. F., Nadirov, R. S., Bagirov, E. B., & Lerche, I. (1997). Geohistory, thermal history
1239 and hydrocarbon generation history of the north-west South Caspian Basin. *Marine and*
1240 *Petroleum Geology*, 14(4), 363–382. [https://doi.org/10.1016/S0264-8172\(96\)00053-0](https://doi.org/10.1016/S0264-8172(96)00053-0)
- 1241 Tingay, M., Heidbach, O., Davies, R., & Swarbrick, R. (2008). Triggering of the Lusi mud
1242 eruption: Earthquake versus drilling initiation. *Geology*, 36(8), 639–642.
1243 <https://doi.org/10.1130/G24697A.1>
- 1244 Tingay, M., Manga, M., Rudolph, M. L., & Davies, R. (2017). An alternative review of facts,

- 1245 coincidences and past and future studies of the Lusi eruption. *Marine and Petroleum*
1246 *Geology*, (December). <https://doi.org/10.1016/j.marpetgeo.2017.12.031>
- 1247 Tingay, M. R. P., Rudolph, M. L., Manga, M., Davies, R. J., & Wang, C.-Y. (2015). Initiation of
1248 the Lusi mudflow disaster. *Nature Geoscience*, 8(7), 493–494.
1249 <https://doi.org/10.1038/ngeo2472>
- 1250 Torrance, J. K. (2010). Shear resistance of remoulded soils by viscometric and fall-cone
1251 methods: a comparison for the Canadian sensitive marine clays. *Canadian Geotechnical*
1252 *Journal*, 24(2), 318–322. <https://doi.org/10.1139/t87-037>
- 1253 Tryggvason, G. (2011). Direct Numerical Simulations of Multiphase Flows: An Introduction.
1254 Retrieved September 24, 2019, from <https://www3.nd.edu/~gtryggva/MultiphaseDNS/>
- 1255 Tryggvason, G., Scardovelli, R., & Zaleski, S. (2011). *Direct Numerical Simulations of Gas-*
1256 *Liquid Multiphase Flows*. Cambridge university press.
- 1257 Tryggvason, Gretar. (2012). *A Front-tracking/Finite-Volume Navier-Stokes Solver for Direct*
1258 *Numerical Simulations of Multiphase Flows*.
- 1259 Tryggvason, Gretar, Esmaeeli, A., Lu, J., & Biswas, S. (2006). Direct numerical simulations of
1260 gas / liquid multiphase flows Direct numerical simulations of gas / liquid multiphase flows.
1261 *Fluid Dynamics Research*, 38, 660–681. <https://doi.org/10.1016/j.fluiddyn.2005.08.006>
- 1262 Unterseh, S., & Contet, J. (2015). Integrated geohazards assessments offshore Azerbaijan,
1263 Caspian Sea. *Offshore Technology Conference, OTC-25911*(May), 1–8.
1264 <https://doi.org/10.4043/25911-MS>
- 1265 Vincent, S. J., Davies, C. E., Richards, K., & Aliyeva, E. (2010). Contrasting Pliocene fluvial
1266 depositional systems within the rapidly subsiding South Caspian Basin; a case study of the
1267 palaeo-Volga and palaeo-Kura river systems in the Surakhany Suite, Upper Productive
1268 Series, onshore Azerbaijan. *Marine and Petroleum Geology*, 27(10), 2079–2106.
1269 <https://doi.org/10.1016/j.marpetgeo.2010.09.007>
- 1270 Wibberley, C. A. J., Yielding, G., & Di Toro, G. (2008). Recent advances in the understanding
1271 of fault zone internal structure: a review. *Geological Society, London, Special Publications*,
1272 299(1), 5–33. <https://doi.org/10.1144/sp299.2>
- 1273 Wibberley, C. A. J., Gonzalez-Dunia, J., & Billon, O. (2017). Faults as barriers or channels to
1274 production-related flow: insights from case studies. *Petroleum Geoscience*, 23(1), 134–147.
1275 <https://doi.org/10.1144/petgeo2016-057>
- 1276 Woolsey, S., McCallum, M. E., & Schumm, S. A. (1975). Modeling of Diatreme Emplacement,
1277 29–42.
- 1278 Wu, K., & Olson, J. E. (2015). Simultaneous Multifracture Treatments : Fully Coupled Fluid
1279 Flow and Fracture Mechanics for Horizontal Wells. In *SPE Annual Technical Conference*
1280 *and Exhibition* (pp. 337–346). New Orleans: Society of Petroleum Engineers.

1281 Zoporowski, A., & Miller, S. A. (2009). Modelling eruption cycles and decay of mud volcanoes.
1282 *Marine and Petroleum Geology*, 26(9), 1879–1887.
1283 <https://doi.org/10.1016/j.marpetgeo.2009.03.003>